

## Path planning in uncertain flow fields using ensemble method

Tong Wang · Olivier P. Le Maître · Ibrahim Hoteit · Omar M. Knio

Received: date / Accepted: date

**Abstract** An ensemble-based approach is developed to conduct optimal path planning in unsteady ocean currents under uncertainty. We focus our attention on two-dimensional steady and unsteady uncertain flows, and adopt a sampling methodology that is well suited to operational forecasts, where an ensemble of deterministic predictions is used to model and quantify uncertainty. In an operational setting, much about dynamics, topography and forcing of the ocean environment is uncertain. To address this uncertainty, the flow field is parametrized using a finite number of independent canonical random variables with known densities, and the ensemble is generated by sampling these variables. For each of the resulting realizations of the uncertain current field, we predict the path that minimizes the travel time by solving a boundary value problem (BVP), based on the Pontryagin maximum principle. A family of backward-in-time trajectories starting at the end position is used to generate suitable initial values for the BVP solver. This allows us to examine and analyze the performance of the sampling strategy, and to develop insight into extensions dealing with general circulation ocean models. In particular, the ensemble method enables us to perform a statistical analysis of travel times, and consequently develop a path planning approach that accounts for these statistics. The proposed methodology is tested for a number of scenarios. We first validate our algorithms by reproducing simple canonical solutions, and then demonstrate our approach in more complex flow fields, including idealized, steady and unsteady double-gyre flows.

**Keywords** Optimal path planning · Heading control · Ensemble forecast · Polynomial Chaos

---

T. Wang · I. Hoteit · O. M. Knio  
Division of Computer, Electrical and Mathematical Sciences and Engineering, King Abdullah University of Science and Technology, Thuwal, Saudi Arabia  
E-mail: Omar.Knio@kaust.edu.sa  
O. P. Le Maître  
LIMSI-CNRS, BP 133, 91403 Orsay, France

## 1 Introduction

Autonomous vehicles, including unmanned air vehicles (UAVs), autonomous underwater vehicles (AUVs), and autonomous surface (ASVs) vehicles, are playing an increasingly important role in both industrial and military applications, with the capability of executing complex search, rescue, surveillance or monitoring missions with minimal operator supervision. In this paper, we focus on AUVs, which are providing key capabilities for ocean monitoring and sampling as well as optimizing the exploitation of marine resources (Adhami-Mirhosseini et al. 2014; Bovio et al. 2006; Marani et al. 2009; Marino et al. 2015; Smith and Huynh 2014; Wang et al. 2009).

One of the main limitations facing the deployments of autonomous vehicles concerns their endurance, due to the limited fuel or battery that they can carry. On the other hand, significant energy is available from the environment mainly through vertical flow motion and spatial velocity gradients in the ocean currents or atmosphere. If these energy sources can be exploited effectively, the speed and range of vehicles would be greatly improved and the mission duration be increased. Path planning aims at using available information about the environment in order ensure optimal utilization of available resources. For instance, the planning may attempt to execute a path in such a way as to reach a target destination as quickly as possible. The cost during the movement of the vehicle depends on the prevailing currents, and is generally variable in space and time. In the underwater scenario, the local conditions can vary appreciably over relatively short periods of time and over short spatial scales (Isern-González et al. 2012). A particular concern arises during “strong currents,” characterized by velocities that are comparable to or even greater than the speed of vehicles. In these situations, one must avoid or minimize the risk of the vehicles becoming trapped or overwhelmed by the current. A variety of path planning approaches have been developed to address these challenges (Garau et al. 2005; Kothari and Postlethwaite 2013; Lermusiaux et al. 2014; Lolla et al. 2012, 2014a,b; Pétrès et al. 2007; Rao 2009; Rhoads et al. 2010, 2013; Soullignac 2011). Traditionally, most of the literature has assumed that the local topography is known and that an accurate current forecast is available. An overview of existing methods falling in this framework is given in Section 2.

However, oceans are extremely complex dynamic systems, and much about the dynamics and topography is uncertain. There are inevitable differences between the actual values (unknown) and the models of physical fields and properties, which compound fundamental limitations on the predictability for nonlinear dynamics (Lermusiaux et al. 2006). In extremely strong currents that are subject to large uncertainty, the predicted fastest path may become unrealizable, that is, the vehicle can not be hold on the path regardless of the control or navigation laws utilized. Conversely, less optimal paths could carry lower risk. One must consequently seek a balance between optimality and level of certainty (Lermusiaux et al. 2014). So far, path planning in spatially complex, strong, time-varying ocean currents under uncertainty has received comparatively less attention than in deterministic settings.

Motivated by the challenges outlined above, we address the path planning problem in an idealized setting, nonetheless involving spatially complex, strong, time-varying ocean currents under uncertainty. Due to the uncertainties in both current direction and magnitude, a single path produced by a model simulation

has limited utility. To overcome this limitation, we follow an approach inspired by operational forecasts, which rely on a finite-size ensemble to quantify uncertainty. Specifically, we follow a methodology based on the generation of multiple optimal paths corresponding to individual realizations of an uncertain current field. The latter is parametrized using a finite number of independent canonical random variables with known densities, and the ensemble is generated by sampling these variables. This enables us to perform a statistical analysis of travel times, and consequently develop a path planning approach that accounts for these statistics.

Due to the limited experience in path planning through realistically complex time-dependent flow fields with uncertainty, we focus our attention on a simplified 2D setting, and restrict our analysis to a well-established path planning methodology. Specifically, we consider a finite-size ensemble of flow realizations, and for each member of the ensemble we solve a boundary value problem (BVP) to determine the corresponding time-optimal path. The formulation of the BVP is based on the Pontryagin maximum principle. A family of backward-in-time trajectories starting at the end position is used to generate suitable initial values for the BVP solver. The present approach readily yields an ensemble of deterministic paths, whose suitability is subsequently examined based on a statistical analysis. Because the individual paths are determined based on deterministic realizations of the flow, this approach enables us to avoid fundamental questions regarding the realizability of the current representation, and consequently focus on analyzing the performance of the sampling strategy, and on developing experiences for follow-on studies dealing with operational general circulation ocean models.

This paper is organized as follows. In section 2, we review prior results on robotic and underwater path planning and briefly discuss control strategies. Section 3 outlines our approach to the determination of a time-optimal path in a deterministic setting, i.e. for an individual realization of the uncertain flow. Section 4 discusses the representation of the uncertainty of flow field, and introduces the ensemble approach to the generation of statistical distributions of the travel time of realizable paths. Application of the methodology is illustrated in section 5, based on simulations of canonical steady and unsteady flows, including weak and strong currents. Major conclusions are summarized in section 6.

## 2 Background

A variety of strategies have been developed to plan safe and optimal paths for general robots, including indirect and direct approaches. In an indirect approach, techniques of calculus of variations (Liberzon 2012) are employed to determine the first-order optimality conditions of the original optimal problem based on the Pontryagin maximum principle. Introducing the Lagrange multipliers (costates) leads to a  $2n$ -dimensional two-point BVP, involving  $n$  state variables and  $n$  costate variables. The optimal trajectories are determined by solving this problem subject to suitable end conditions. The main difficulty with this approach is to find a first estimate of the unspecified conditions at one end that produces a solution reasonably close to the specified conditions at the other end. The reason for this peculiar difficulty is that the optimal solutions are often very sensitive to small changes in the unspecified boundary conditions, i.e., the values of initial costates (Bryson and Ho 1975; Betts 1998). As a result, when the indirect approach is considered, the

initial value for costates should be well chosen. By solving a dynamic Hamilton Jacobi Bellman (HJB) partial differential equation (PDE) for the time-varying optimal time-to-go function and the associated optimal control law, Rhoads et al. (2010, 2013) obtain globally optimal trajectories for fixed speed AUVs in known, 2D, spatially complex, time-dependent flow fields. For a constant-speed UAV flying at constant altitude in steady uniform winds, Techy and Woolsey (2009) provide a simple analytical solution for a subset of candidate extremal paths.

The fast marching (FM) methods, very similar to Dijkstra’s method but allowing continuously variable direction of motion, have also been applied to include the case of underwater path planning. The FM methods solve an Eikonal equation, a simple case of the HJB PDE, to track a propagating interface, and find the arrival time function of points in the space at isotropic speed of propagation (Sethian 1999a; Gómez et al. 2013). Ordered upwind methods (OUMs) generalize FM methods from isotropic problem to general anisotropic problem. OUMs develop methods for approximating the solutions to a wide class of static HJB PDEs (Sethian and Vladimirovsky 2001, 2003). A heuristically guided version of OUMs referred to the FM\* algorithm is developed in Pétrès et al. (2007), especially for the application of AUVs. Another method to track interface motion implicitly, introduced by Sethian (1999b), is the Level Set Method; it provides a straightforward approach to solve initial value PDE for the level set function in the entire computational space. Lolla et al. (2012, 2014a,b) use level set methods to predict the time-optimal paths of AUVs navigating in continuous, strong, and dynamic ocean currents, and predict collision-free and minimum-time trajectories for swarms of AUVs deployed in the Philippine Archipelago region respectively. Voronoi diagrams have also been employed to interpret the minimum travel time problem between two given points in the current (Bakolas and Tsiotras 2010).

In direct methods, either states or controls, or both states and controls are discretized and the continuous optimal control problem is converted to a nonlinear parameter optimization problem. While seemingly unrelated, these two approaches have much in common, and various techniques do not fall squarely into one category or another (Rao 2009). Graph search techniques are mostly used in path planning for both AUVs and UAVs; examples include dynamic programming-based approaches such as the so-called wavefront expansion and A\* method (Eichhorn 2015; Garau et al. 2005; Smith and Huynh 2014; Soullignac 2011; Wu et al. 2011). These algorithms are commonly criticized for the grid and the discrete state transitions, which constrain the motion of the vehicle to limited directions. In addition to this limitation, optimality may be compromised due to graph discretization alone. In continuous, complex marine environments, the graph search approaches are computationally expensive and may lead to infeasible paths. Rapidly exploring random trees (RRTs) randomly build a space-filling tree and then search nonconvex, high-dimensional spaces. Their ability to handle problems with obstacles and different constraints has led to the widespread use in path-planning applications including ocean cases (Rao and Williams 2009) and wind environment (Kothari and Postlethwaite 2013).

Once a path has been selected, it is critical that the AUVs be capable to follow these paths with good accuracy. Path-following approaches are frequently used for this purpose. Unlike standard trajectory tracking, in a path following approach no restrictions are placed on the temporal propagation along paths. A fundamental difference between standard trajectory-tracking and path-following concerns

performance limitations due to unstable zero-dynamics, which can be removed in path-following approach (Aguiar et al. 2005, 2008; Aguiar and Hespanha 2007). Path-following generally aims at controlling the forward speed to track a desired profile, as well as the orientation of the vehicle to drive it onto the path.

Different controllers are designed to guarantee asymptotic convergence to the path. Path-following controllers for UAVs have been reported in Kaminer et al. (2010); Sujit et al. (2014); Xargay et al. (2013). For AUVs, Lapierre and Jouvenel (2008) derive a kinematic controller first and extend it to cope with vehicle dynamics by resorting to backstepping and Lyapunov-based techniques. The resulting nonlinear adaptive controller yields asymptotic convergence of the vehicle to the path at a constant speed. Ghabchelloo et al. (2009) address the problem of steering a group of vehicles along given spatial paths while holding a desired time-varying geometrical formation pattern. Aguiar and Pascoal (2007) consider the problem of dynamic positioning and way-point tracking of underactuated AUVs, in the presence of constant unknown ocean currents and vehicle parametric uncertainty.

In contrast to deterministic settings, prior experiences on path planning in realistically-complex, time-dependent, uncertain flow fields are limited. Difficulties arise due to chronic undersampling of the oceans, the complexity of ocean processes that lead to limitations on the accuracy of ocean predictions, the inevitable differences between the actual values (unknown) and the measured or modelled values of physical fields and properties, as well as fundamental restrictions on predictability for nonlinear dynamics (Lermusiaux et al. 2006). Thus, the practical horizon for skillful forecasts that can be used to plan optimal paths is also limited, and one must seek a balance between optimality and risk (Lermusiaux et al. 2014). Recently, to improve the safety and reliability of AUV operation in coastal regions, Pereira et al. (2013) propose two stochastic planners, a Minimum Expected Risk planner and a risk-aware Markov Decision Process, both of which have the ability to utilize ocean current predictions in a probabilistic manner.

Ensemble forecast has been standard in modelling uncertainties in climate and ocean simulations (Constantinescu et al. 2011; Leutbecher and Palmer 2008; Murphy et al. 2004; Evensen 2003; Hoteit et al. 2013; Höllt et al. 2015). Dynamically Orthogonal (DO) stochastic PDEs, generalized polynomial chaos and other techniques have also been used to predict uncertainties in engineering applications and environmental flows (Le Maître and Knio 2010; Sapsis and Lermusiaux 2009, 2012; Alexanderian et al. 2012; Sraj et al. 2013, 2014a,b). Wolf et al. (2010) utilized a Markov decision process to integrate the uncertainty of the wind field in both direction and magnitude components into the wind model and planned probabilistic motion for Montgolfieré balloons in the atmosphere of Titan to reach a goal location through the uncertain wind field in the fastest expected time. Bakolas and Tsiotras (2012) divided the temporally, spatially varying drift field induced by local winds/currents into two parts, the one which is perfectly known to the agent and the other that is unknown and assumed to be a piecewise continuous function of time. According to the fidelity of the information about the local drift available to the agent, that is, an aerial or marine vehicle, several navigation schemes are presented and appropriately tailored.

### 3 Time-optimal path planning in a deterministic flow field

Our approach to time-optimal path planning is based on the use of well-established methodologies that are applied to individual realization of the flow field (Bryson and Ho 1975; Betts 1998; Fainshil and Margaliot 2012; Laschov and Margaliot 2013; Liberzon 2012; Lifshitz and Weiss 2015; Ohsawa 2015). We specifically rely on the Pontryagin maximum principle to formulate the problem as a free-time, fixed-endpoint boundary value problem (BVP). In order to provide reasonable initial guesses for the BVP solver, a family of backward-in-time trajectories is computed, starting at the end position but with different headings. This section outlines these approaches, and summarizes a simplified technique to determine a path-following control law. We conclude by providing brief highlights of a preliminary computational study focusing on validating the predictions of the solution algorithm.

#### 3.1 Problem Statement

Consider a vehicle ( $G$ ) moving under the influence of a flow field in an unsteady ocean current,  $\mathbf{u}(\mathbf{x}, t)$ . The problem of interest is to estimate a control law for  $G$  that minimizes the travel time from a given starting position  $\mathbf{x}_0 = (x_0, y_0)$  at time  $t_0$  to a fixed end position  $\mathbf{x}_f = (x_f, y_f)$ . We will restrict our attention to two-dimensional flow fields, and to the situation where the vehicle speed,  $V$ , with respect to the current is constant. In other words, the goal is to determine a steering rule that results in the fastest path from  $\mathbf{x}_0$  to  $\mathbf{x}_f$ .

Given a deterministic flow field, let  $\mathbf{X}_T$  denote a continuous trajectory from  $\mathbf{x}_0$  to  $\mathbf{x}_f$  (see Fig. 1). The vehicle motion is composed of two velocity vectors, the relative motion due to steering and advection induced by the local current. Thus, the total velocity of  $G$  can be expressed as:

$$\frac{d\mathbf{X}_T}{dt} = \mathbf{U}(\mathbf{X}_T, t) = V\hat{\mathbf{h}}(t) + \mathbf{u}(\mathbf{X}_T, t), \quad (1)$$

where  $V$  is the (fixed) speed of the vehicle, the control input  $\hat{\mathbf{h}}(t)$  is the heading (unit) vector, and  $\mathbf{U}(\mathbf{X}_T, t)$  is the local velocity of the current. The limiting conditions on the trajectory  $\mathbf{X}_T$  are

$$\mathbf{X}_T(\mathbf{x}, t_0) = \mathbf{x}_0, \quad \mathbf{X}_T(\mathbf{x}, t_f) = \mathbf{x}_f. \quad (2)$$

In component form, the equation of motion can be expressed as:

$$\frac{dx}{dt} = u(x, y, t) + V \cos \theta(t), \quad \frac{dy}{dt} = v(x, y, t) + V \sin \theta(t), \quad (3)$$

where  $u$  and  $v$  are the components of  $\mathbf{u}$ , and  $\theta(t)$  is the instantaneous angle associated with the heading, i.e.  $\hat{\mathbf{h}}(t) = (\cos \theta(t), \sin \theta(t))$ .

In the present setting, our goal is to find the optimal control  $\theta^*(t)$  and the resulting state trajectory  $\mathbf{X}_T^*$  subject to kinematic relation (1) and the limiting conditions (2) that minimize the cost function

$$\int_{t_0}^{t_f} 1 dt = t_f - t_0. \quad (4)$$

### 3.2 Formulation as BVP

We rely on the Pontryagin maximum principle to obtain the necessary conditions for a controlled trajectory to be optimal under the stated constraints. To this end, we introduce the Hamiltonian associated to the kinematic constraint (1) and the performance measure (4),

$$H(x, y, t, \theta, p_1, p_2) \equiv 1 + p_1 \frac{dx}{dt} + p_2 \frac{dy}{dt}, \quad (5)$$

where  $p_1 \equiv p_1(x, y, t)$  and  $p_2 \equiv p_2(x, y, t)$  are costates. For the present setting, the optimal state trajectory  $(x^*, y^*)$  and costate trajectory  $(p_1^*, p_2^*)$  satisfy the canonical equations (Liberzon 2012):

$$\dot{x}^* = \partial H^* / \partial p_1, \quad \dot{y}^* = \partial H^* / \partial p_2, \quad (6)$$

$$\dot{p}_1^* = -\partial H^* / \partial x, \quad \dot{p}_2^* = -\partial H^* / \partial y, \quad (7)$$

with the boundary conditions  $(x^*(t_0), y^*(t_0)) = (x_0, y_0)$ ,  $(x^*(t_f), y^*(t_f)) = (x_f, y_f)$ . The state's and costate's explicit dependences on the (unknown) final time,  $t_f$ , can be removed by introducing the scaled time variable  $\tau \equiv t/t_f$ , so that when normalized accordingly the BVP (Eq. 6 and 7) has to be solved in the unit interval  $0 \leq \tau \leq 1$  (Longuski et al. 2014). Thus,  $t_f$  is treated as a variable, which must be determined as part of the optimal solution.

On the optimal trajectory  $\mathbf{X}_T^*$ , the necessary condition for optimality is expressed as:

$$\frac{\partial H^*}{\partial \theta} = 0, \quad (8)$$

where  $H^* \equiv H(x^*, y^*, t, \theta^*, p_1^*, p_2^*)$ . Together with the kinematic relation Eq. (3), this leads to the following relationship between steering law  $\theta^*$  and the costates:

$$-p_1 \sin \theta^* + p_2 \cos \theta^* = 0. \quad (9)$$

In the computations below, we rely on the Matlab solver `bvp4c` to determine the optimal solution. The solver requires initial guesses for the travel time,  $t_f$ , and the costates  $p_1^*(t_0)$  and  $p_2^*(t_0)$ . Starting from these guesses, the solver determines the optimal solution through iterative updates. The quality of guesses is critical for a successful computation and for the solver performance. Finding reasonable guesses is a delicate issue, because the neighbourhood of the initial costates at the starting position for which the algorithm converges to the optimal solution is small. To address this issue, a family of backward-in-time trajectories starting at the end position with different headings is generated in order to determine reasonable initial guesses for the solver.

### 3.3 Backward integration

If the vehicle reaches the end position at the (yet unspecified) final time,  $t_f$ , in optimal fashion, i.e.,  $\mathbf{X}_T^*(\mathbf{x}, t_f) = \mathbf{x}_f$ , the terminal condition

$$H(x_f, y_f, t_f, \theta_f, p_{1,f}, p_{2,f}) = 0 \quad (10)$$

must be satisfied. This leads to:

$$1 + p_{1,f} (u_f + V \cos \theta_f) + p_{2,f} (v_f + V \sin \theta_f) = 0, \quad (11)$$

where  $(p_{1,f}, p_{2,f})$  is the costate at the final time and end position, i.e.,  $p_{1,f} \equiv p_1(x_f, y_f, t_f)$  and  $p_{2,f} \equiv p_2(x_f, y_f, t_f)$ . Letting  $\theta_f$  denote the heading of the vehicle at the end position,  $u_f \equiv u(x_f, y_f, t_f)$ ,  $v_f \equiv v(x_f, y_f, t_f)$ , using Eq. (9) we obtain:

$$p_{1,f} \sin \theta_f = p_{2,f} \cos \theta_f. \quad (12)$$

Combining the above two equalities results in:

$$p_{1,f} = \frac{-\cos \theta_f}{u_f \cos \theta_f + v_f \sin \theta_f + V}, \quad p_{2,f} = \frac{-\sin \theta_f}{u_f \cos \theta_f + v_f \sin \theta_f + V}. \quad (13)$$

Thus, if the heading  $\theta_f$  is specified, the above two equations can be used to determine  $p_{1,f}$  and  $p_{2,f}$ , and consequently a complete set of initial values is obtained that is necessary for integrating the coupled system consisting of Eqs. (1) and (7) backward in time.

In the computations, we generate a family of backward-in-time trajectories starting at the end position by considering different headings,  $\theta_f$ . To this end, we discretize the interval  $(0, 2\pi)$  using a fine mesh, and consider all admissible headings belonging to the set of discrete nodes. The backward integration is carried out over a sufficiently large time horizon,  $T^{max}$  (see Appendix). In the time-dependent case, because  $\theta_f$  and  $t_f$  are both unknown, one cannot generally guarantee that the backward trajectory which comes closest to  $\mathbf{x}_0$  does so at time  $t_0$ . In addition, one must provide a guess,  $\bar{t}_f$ , for the final time so that the backward integration is suitably initialized. In the computations, we start with the initial guess,  $\bar{t}_f = t_0 + T^{max}$ , and then reduce smaller values if the iterations do not lead to suitable guesses for the costates. Note that, as in the steady current case, the backward trajectories only used to generate initial guesses for the costates, and the value of  $t_f$  is actually determined as part of the iterative solution of the BVP problem, and subsequently verified by forward integration. Also note that consideration of large value of  $T^{max}$  helps ensure that the collection of backward trajectories can yield suitable values of initial guesses.

From the resulting family of backward-in-time solutions, we select the trajectory that comes closest to the starting point in order to generate initial guesses for the BVP solver. First, the point on this trajectory coming closest to the starting point is selected to draw the initial guess for the costate vector. Then the solution given by the BVP solver is verified by substituting the resulting control input into Eqs. (1) and integrating the system forward in time from time  $t_0$ , and the starting point  $\mathbf{x}_0$ . The solutions obtained by the BVP solution and by forward integration are then contrasted. In a case of a large discrepancy, namely greater than a small threshold distance set to 0.08, neighboring points upstream and downstream of the initial guess are selected. Additional guesses are generated, as needed, until the discrepancy drops below the specified threshold. This verification step is helpful to avoid difficulties when the iterative BVP solver fails to provide a converged solution or to detect conditions when the solution converges to a local optimum.

### 3.4 Path following control law

In addition to determination and verification of optimal paths in a deterministic flow, one needs to address the question of whether the vehicle is able to follow a predefined path that does not coincide with the optimal solution.

To address this question, a simplified approach is developed in this section to assess whether a specified path is realizable in a given velocity field, and in this case of the time required to travel along this path. Specifically, we seek to determine the control law  $\theta(t)$  that guides the vehicle along the specified path  $\mathbf{X}_P$ .

The present approach is based on discretizing the path using a collection of  $M$  points,  $(x_l, y_l)_{l=1}^M$ , lying on the corresponding curve. The points are indexed using an approximate arc-length variable,  $s$ , defined according to:

$$s_l = s_{l-1} + \frac{\Delta_l}{L}, l = 2, \dots, M \quad (14)$$

where  $s_1 = 0$ ,  $\Delta_l \equiv \sqrt{(x_l - x_{l-1})^2 + (y_l - y_{l-1})^2}$ ,  $l = 2, \dots, M$ , and  $L = \sum_{i=2}^M \Delta_i$ . This parametrization can be readily exploited to define the local tangent,  $\hat{\mathbf{t}}$ , and normal,  $\hat{\mathbf{n}}$ , to the path. Second-order finite differences are used for this purpose.

Let  $\gamma$  denote the angle along  $\hat{\mathbf{t}}$  with respect to the  $x$ -axis (see Fig. 2). On the specified path, the total velocity of the vehicle,  $\mathbf{U}(\mathbf{x}, t) = (u + V \cos \theta(t), v + V \sin \theta(t))$ , must point in the  $\hat{\mathbf{t}}$  direction, and the component of total velocity along  $\hat{\mathbf{n}}$  must be zero, i.e.

$$\cos \gamma (v + V \sin \theta) - \sin \gamma (u + V \cos \theta) = 0,$$

which results in:

$$V \sin(\theta - \gamma) = u \sin \gamma - v \cos \gamma. \quad (15)$$

Equation (15) could have no solution, one solution, or two solutions, depending on the relative velocity of the vehicle with respect to that of the current (see Fig. 3), or alternatively according to the value of  $c \equiv (u \sin \gamma - v \cos \gamma)/V$ . Specifically, we have:

- (a) If  $|c| > 1$ , no solution exists. In this case, the specified path is deemed unrealizable in the local flow field. We characterize this scenario by setting the arrival time to  $\infty$ .
- (b) If  $|c| \leq 1$ ,  $\theta$  has one solution or two solutions, given by:

$$\theta = \gamma + \arcsin(c), \quad (16)$$

and

$$\theta = \gamma + \pi - \arcsin(c), \quad (17)$$

Note, however, that the total velocity of the vehicle  $\mathbf{U}(x, y, t)$  must point in the direction of  $\hat{\mathbf{t}}$ , i.e., the condition

$$(u + V \cos \theta) \cos \gamma + (v + V \sin \theta) \sin \gamma \geq 0 \quad (18)$$

must be satisfied. Thus, the solutions in (16) and (17) are admissible depending on whether the condition (18) is satisfied. When two solutions exist, each branch is maintained until the condition in (18) is no longer satisfied, point at which switching from one branch to another is considered. This may result in multiple control laws leading from the starting to end positions. When this is the case, the solution resulting in the smallest travel time is selected.

Once a suitable control law,  $\theta(t)$ , is determined, the travel time along the specified path may be readily required based on  $\theta$  and the parametrized representation of the path. Specifically, letting  $\mathbf{x}$  denote the position of the vehicle and  $s$  denote a parametrization variable of the path, a straightforward manipulation of the kinematic relation,

$$\frac{d\mathbf{x}}{dt} = \frac{d\mathbf{x}}{ds} \cdot \frac{ds}{dt}, \quad (19)$$

results in:

$$\frac{ds}{dt} = f(s) \doteq \frac{|d\mathbf{x}/dt|}{|d\mathbf{x}/ds|}. \quad (20)$$

Note that in the definition of  $f$ , the numerator is determined once  $\theta$  is specified, whereas the denominator can be readily obtained by differentiating the parametrized representation of the path. As with the tangent vector, second-order differences are used for estimating  $\partial\mathbf{x}/\partial s$ . Consequently, the total travel time may be estimated from:

$$\int_{t_0}^{t_f} dt = \int_{s_1}^{s_M} \frac{ds}{f(s)}. \quad (21)$$

A numerical quadrature based on the composite trapezoidal rule is used to estimate the integral on the right-hand side of Eq. (21).

### 3.5 Illustration

A variety of scenarios were considered in order to verify the predictions of the core algorithm. In this section, we provide a brief illustration of one example used in the numerical study. The selected example specifically focuses on the case of the time-invariant, spatially double-gyre flow. The current is specified in terms of its velocity components, namely

$$u(x, y) = -\sin(\pi x) \cos(\pi y), \quad v(x, y) = \cos(\pi x) \sin(\pi y). \quad (22)$$

To illustrate our solution procedure, we plot in Fig. 4 a selected subset of backward in time trajectories. A total of 360 trajectories is computed, but only 24 are shown. This ensemble is determined by varying the final approach angle with a one degree increment. The point closest to the starting position  $\mathbf{x}_0 = (-1, -0.25)$  in the entire family is determined; it is identified using a (+) sign in the figure. This is achieved by monitoring the minimum distance between the starting point and each of the individual backward-in-time paths, as illustrated in Fig. 5. The local values of  $p_1, p_2$  at this point are then used as initial guesses for the bvp solver. If an optimal solution is not found using these guesses, values at neighboring points are considered. Once suitable initial guesses for  $p_1, p_2$  and the travel time are provided, the bvp solver provides both the optimal trajectory together with the optimal control law. To verify the predictions, the optimal control law is used to recompute the trajectory using forward in time integration. Solutions are deemed acceptable when the peak distance between instantaneous positions falls below the specified tolerance.

Figure 6 shows three optimal trajectories and the corresponding optimal control inputs in a close up of the flow field. The problem parameters are the same as in Rhoads et al. (2013). In all cases, the vehicle starting position at  $t = 0$ ,

$(x_0, y_0) = (0.5, 0.5)$ , coincides with the center of a gyre. The vehicle velocity,  $V = 0.75$ , is smaller than the peak current velocity,  $u_{\max} = 1$ . Three target positions are considered, namely  $(2.5, 0.5)$ ,  $(2.25, 1.5)$ , and  $(1.5, 2.25)$ . On the optimal trajectory, the vehicle takes advantage of the flow in a way that minimizes the arrival time. The results predicted by the present algorithm are in close agreement with those reported in Rhoads et al. (2013). In addition, the trajectories computed through forward integration of the equations of motion with the control input determined through the solution of the BVP are essentially identical. This provides confidence in the predictions of the present algorithm.

#### 4 Path planning under uncertainty

We adopt a probabilistic framework to represent uncertainty in the current field. To this end, variability in the velocity field is represented in terms of a  $d$ -dimensional random vector,  $\boldsymbol{\xi}$ , and expressed according to:

$$\mathbf{u}(\mathbf{x}, t, \boldsymbol{\xi}) = (u(\mathbf{x}, t, \boldsymbol{\xi}), v(\mathbf{x}, t, \boldsymbol{\xi})), \quad (23)$$

where  $\mathbf{x} = (x, y)$  is the location, and  $t$  is time. Without loss of generality, the components of  $\boldsymbol{\xi}$  are assumed to be independent and identically distributed (iid), with uniform distribution over  $[-1, 1]$ .

Within this framework, we explore an *approximate* approach to path planning in uncertain flows. The development is guided by multiple considerations, including a desire to mimic the scenario with operational ocean forecasts, which rely on computing a finite ensemble of predictions, and on using these predictions to represent the underlying variability of the ocean current. An additional consideration concerns our desire to re-use deterministic path planning techniques, and to limit the full application of the optimal planning algorithm to a manageable number of current realizations.

Based on the considerations above, the presently explored approach is outlined as follows. We start by generating a “design” ensemble of current realizations. A Latin Hypercube Sampling (LHS) strategy is used for this purpose McKay et al. (1979); Le Maître and Knio (2010). It is implemented by generating pseudo-random samples of the germ,  $\boldsymbol{\xi}$ , and substituting the resulting samples into the velocity field representation in (23). The size of the initial ensemble thus generated is denoted  $N_i$ . In other words, the starting point in the uncertainty analysis consists in an ensemble of velocity fields,  $\mathbf{u}_i \equiv \mathbf{u}(\mathbf{x}, t, \boldsymbol{\xi}_i)$ ,  $i = 1, \dots, N_i$ .

For each member of the initial current ensemble, the deterministic optimal path planning algorithm is applied, resulting in an ensemble of paths,  $p_i$ ,  $i = 1, \dots, N_i$ . The next step in the analysis is to determine whether or not these paths remain realizable when tested against other members of the initial current field ensemble. To this end, the path following algorithm is applied for each combination of path,  $p_i$ , and current,  $\mathbf{u}_j$ ,  $1 \leq i, j \leq N_i$ . When a path is not realizable for a particular current sample, it is simply dropped from further analysis. On the other hand, when a path remains realizable, one readily obtains an estimate of the arrival time for all members of the ensemble.

The last step of the analysis is based on drawing independent ensembles of the current field, again using LHS. We consider larger ensembles, namely with size  $N_l > N_i$ . The ensemble of paths  $p_i$  are tested against members of the larger

ensembles, potentially leading to further decrease in the number of realizable paths. The end result consists of an ensemble of paths that are all realizable for all members of the initial and independent current field ensembles. The realizable paths are denoted  $p_i^r$ ,  $i \in J \subset \{1, \dots, N_i\}$ . The size of the ensemble of realizable paths is denoted by  $N_r$ , with  $N_r \leq N_i$ . In other words,  $J$  has cardinality  $N_r$ .

This machinery readily yields, for each realizable path  $p_i^r$ , a collection of arrival times  $T_{i,j}$ ,  $i \in J$ ,  $j = 1, \dots, N_l$ . This, in turns, enables us to characterize the statistics of the corresponding arrival times in the uncertain current. In the computations below, for each  $i \in J$ , we estimate the mean,

$$\bar{T}_i = \frac{1}{N_l} \sum_{j=1}^{N_l} T_{i,j}, \quad (24)$$

the standard deviation,

$$\sigma_i = \sqrt{\frac{1}{N_l} \sum_{j=1}^{N_l} (T_{i,j} - \bar{T}_i)^2}, \quad (25)$$

the worst case value,

$$T_i^{worst} = \max_{j=1, \dots, N_l} (T_{i,j}), \quad (26)$$

and the value at risk based on a 95% probability. The latter is denoted as  $T^{95\%}$ , and is simply estimated by sorting the arrival time values in ascending order, and selecting the first index that bounds  $0.95N_l$ . Finally, kernel density estimation is used in conjunction with the discrete predictions to visualize the probability density function of the arrival time.

#### 4.1 Remarks

One should first note that the methodology outlined above does not necessarily lead to a global optimum, regardless of the specific metric one aims to minimize. This is the case because the analysis is based on a finite size ensemble of paths. An advantage of the present approach, however, is that it only requires availability of a deterministic path planning algorithm, and that it inherently limits the number of associated inverse solutions. In contrast, once a candidate path is identified, evaluation of the corresponding arrival time statistics can be performed in a systematic and efficient fashion, because the (forward) solutions associated with the path following algorithm are computationally inexpensive.

Of course, suitability of the present approach hinges on whether the moderate size ensemble identified in the initial step provides a suitable representation of the underlying variability of the flow, and that the paths determined as a result of the evaluation also provide a suitable ensemble. For the canonical flows considered in the present study, the initial sampling (with  $N_i = 64$ ) proved suitable in all cases considered. In general, however, the size of the initial sample may need to be tuned according to the complexity of the flow, the constraints and capabilities of the vehicle, and the specifics of the mission. These questions are outside the scope of the present study and will be addressed elsewhere.

## 5 Results and discussion

In this section, we illustrate our path planning algorithm by means of two cases studies. The first case study (section 5.1) specifically focuses on a stochastic, time-invariant, double-gyre flow, with uncertainty in both the direction and magnitude of the current. This generalizes the deterministic setting considered in section 3.5. In the second case study (section 5.2), we consider a more complex setting, consisting in an uncertain, time-dependent, double-gyre flow.

### 5.1 Time-invariant, spatially double-gyre flow field with uncertainty

Let us consider the path-planning problem in the time-invariant, stochastic double gyre flow specified according to:

$$\begin{aligned} u(\mathbf{x}, \boldsymbol{\xi}) &= -\alpha\xi_1 \sin(\pi(x + \delta\xi_2)) \cos(\pi(y + \delta\xi_3)) - \sin(\pi x) \cos(\pi y), \\ v(\mathbf{x}, \boldsymbol{\xi}) &= \alpha\xi_1 \cos(\pi(x + \delta\xi_2)) \sin(\pi(y + \delta\xi_3)) + \cos(\pi x) \sin(\pi y), \end{aligned} \quad (27)$$

with parameters  $0 < \alpha, \delta < 1$ . Thus, the uncertainty in the flow field is represented in terms of a three-dimensional random vector,  $\boldsymbol{\xi}$ . The components of  $\boldsymbol{\xi}$  are assumed to be independent and uniformly distributed over  $[-1, 1]$ . The first coordinate,  $\xi_1$ , represents the impact of an uncertain velocity magnitude, whereas  $\xi_2$  and  $\xi_3$  reflect uncertainty in the location of the gyre. The parameters  $\alpha$  and  $\delta$  quantify the strength of the velocity magnitude and gyre location uncertainties, respectively.

Below we consider two examples, identified according to the vehicle velocity. In the first example,  $V = 0.75$ , so that the vehicle velocity can fall below the peak current velocity. In the second example,  $V = 1.2$ , so the vehicle is always able to fight against the current. In both examples, the initial and final locations of the vehicle are held fixed, respectively  $(t_0, x_0, y_0) = (0, -1, -0.25)$  and  $(x_f, y_f) = (0.5, 0.5)$ . We also set  $\alpha = 0.5$ ,  $\delta = 0.1$ . The Hamiltonian and the adjoint equations are given in Appendix A.

#### 5.1.1 Example 1: small $V$

In this example, we set  $V = 0.75$ , and so the peak magnitude of the current is almost double the vehicle's speed. We use a Latin Hypercube Sampling (LHS) strategy to generate an  $N$ -member ensemble of the random variables,  $\xi_1, \xi_2$ , and  $\xi_3$ , and accordingly of current realizations. We start by considering a 64-member ensemble. The mean velocity vector estimated based on the corresponding samples is shown in Fig. 7. The maximum standard deviation is about 30% of the mean of the individual current velocity maxima. Thus, the variability of the current velocity is substantial.

To assess the impact of uncertainty in the current, we determine the trajectories that minimize the travel time for each member of the ensemble. The deterministic solution algorithm is used for this purpose. This yields an ensemble of paths, having the same size as the ensemble of current realizations. For each of these paths, we then assess the variability of the arrival time with respect to the ensemble of current realizations. Consequently, we obtain discrete distributions of arrival times, with one distribution for each path.

We first note that not all of the individual minimal-time paths can be followed in the whole current ensemble. When a certain individual path cannot be followed under another realization of the current field, this path is deemed unrealizable, and consequently dropped from the subsequent statistical analysis. For the present example, and the present sample, Fig. 8(a) shows that there are only 12 realizable paths in the 64-member ensemble. For all realizable paths, the arrival times computed using the path-following control law (section 3.4) can be readily exploited to characterize the corresponding arrival-time distribution. We specifically determine, for each realizable path, (i) the maximum and minimum travel time,  $T^{worst}$  and  $T^{best}$ , where the maximum and minimum are taken over all current realizations, (ii) the mean travel time,  $\bar{T}$ , again averaging over all current realizations, and (iii) the value at risk,  $T^{95\%}$ . Also plotted are the values lying at  $\pm$  one standard deviation around the mean. Fig. 9 shows the result of travel-time characterization for the 12 realizable paths of the present 64-member current ensemble in Fig. 8(a).

In order to suitably select a path in the uncertain flow field, it is instructive to first examine the robustness of the computed arrival time distribution with respect to the ensemble size. We briefly examine this question by computing the arrival time distribution for the 12 realizable paths in the 64-member current ensemble, using the independent LHS samples of the current field. Specifically, the 12 realizable paths are re-evaluated using 144-member and 256-member ensembles. We note that the best worst case (the first path in Fig. 9) is no longer realizable when the 256-member current ensemble is considered. (Consequently, path 1 is also deemed unrealizable and is dropped from further consideration.) This indicates that a straightforward “robust optimization” approach, selecting best worst case based on a limited size ensemble, may not generally be suitable, particularly because of potential susceptibility to sampling errors.

On the other hand, the paths labelled 2-12 in Fig. 9 all remain realizable for both 144-member and 256-member ensembles. Figure 10(a) shows the characterization of the travel times for these 11 realizable paths in the 64-member, 144-member and 256-member ensemble. Plotted are estimates of the mean arrival time, the corresponding standard deviation,  $\sigma$ , the most likely travel time, and  $T^{95\%}$ . We observe that, as expected, the curves generally exhibit a decreasing trend as the ensemble size increases. Note, however, that the curves of the most likely arrival time value obtained using the 144-member and 256-member ensembles intersect, suggesting that effects of finite sample size are still appreciable. Also note that the minimum values of the mean arrival time, the most likely arrival time, and  $T^{95\%}$ , are all achieved for path 4. It is consequently identified as the path showing the optimal overall performance. The travel time distribution for path 4 is shown in Fig. 10(b). Plotted are curves generated using the 64-member, 144-member, and 256-member ensembles. The results indicate that as the ensemble size increases, the pdfs appears to converge. Specifically, with 144 and 256 members the distributions are close, but significant differences with the 64-member can be observed. The present experiences underscore the need to systematically address the impact of variability in the current field, and to examine the robustness of computed estimates with respect to sample size. They also indicate that a reasonable strategy for path planning in an uncertain flow field can be based on considering a small set of deterministic optimal trajectories based on a limited current ensemble, and further examining the arrival time statistics for increasing ensemble sizes. While this may not result in a global optimum, the approach takes advantage of the

efficiency of the (forward) path-following solves, namely by limiting the computational burden of performing (inverse) path determinations over very large current ensembles.

### 5.1.2 Example 2: large $V$

We now consider a higher vehicle speed,  $V = 1.2$ . In this case, along most of its path the vehicle velocity is larger than that of the current, though the peak current velocity still exceeds that of the vehicle. As in section 5.1.1, a LHS strategy is used to generate a 64-member current ensemble, and the deterministic optimization scheme is applied to determine the path that minimizes the travel time for each realization of the current.

Figure 11 shows the characterization of the travel times along each of the computed paths. We first note that, due to the larger speed of the vehicles, all trajectories remain realizable when tested against members of the same current ensemble. In addition, in the present case the vehicle reaches its target destination in an appreciably shorter time than in the previous case. In particular, it can be seen that with  $V = 0.75$ , in the worst worst case (path 12 in Fig. 9), the vehicle needs a time period of about 2 to reach the target, whereas with  $V = 1.2$  in the worst worst case (path 64 in Fig. 11) the vehicle only requires a period of about 1.25 to complete the corresponding path.

To select a suitable path in the uncertain current field, we first examine the sensitivity of the arrival time estimates to the ensemble size. To this end, the 64 realizable paths are re-evaluated based on two independent ensembles, comprising 144 members and 256 members. We first note that all 64 paths determined in the first ensemble remain realizable when tested using the independent larger-size ensembles. Figure 12(a) shows the characterization of the travel times for the 64 realizable paths in the 64-member and 144-member ensemble. Plotted are estimates of the mean arrival time, the corresponding standard deviation,  $\sigma$ , the most likely travel time, and the value at risk,  $T^{95\%}$ . One notes that, because of the increase in the vehicle's speed, the variability in the current field has lesser impact on the travel time than in the case with small  $V$ . In addition, we find that the travel time estimates obtained in 144-member ensemble and 256-member ensemble are almost identical. Consequently, the travel time estimates obtained using the 256-member ensemble are not plotted.

Based on the results in Fig. 12(a), one observes that path 4 achieves the smallest value at risk,  $T^{95\%} \simeq 1.18$ . The pdf of the arrival time for path 4 is shown in Fig. 12(b). Plotted are curves obtained using all three ensembles. While the effects of finite size ensembles are still evident, one notes that in the present case the range of the distribution is quite small, falling approximately between 1 and 1.25. This is consistent with previous observations concerning diminished impact of the current variability when the vehicle speed is large.

## 5.2 Time-dependent spatially double-gyre flow field with uncertainty

In this section, we consider a more complex case, focusing on unsteady, periodically varying double-gyre flow, which mimics flow patterns observed in the

ocean(Shadden et al. 2005). Specifically, the uncertain current field is expressed as:

$$\begin{aligned} u(\mathbf{x}, t, \boldsymbol{\xi}) &= -\alpha\xi_1 \sin(\pi f(x + \delta\xi_2, t)) \cos(\pi(y + \delta\xi_3)) - \sin(\pi f(x, t)) \cos(\pi y) \\ v(\mathbf{x}, t, \boldsymbol{\xi}) &= \alpha\xi_1 \cos(\pi f(x + \delta\xi_2, t)) \sin(\pi(y + \delta\xi_3)) (2a(t)(x + \delta\xi_2) + b(t)) \\ &\quad + \cos(\pi f(x, t)) \sin(\pi y) (2a(t)x + b(t)) \end{aligned} \quad (28)$$

where

$$f(x, t) = a(t)x^2 + b(t)x, \quad (29)$$

$$a(t) = \epsilon \sin(\omega t), \quad (30)$$

$$b(t) = 1 - 2\epsilon \sin(\omega t). \quad (31)$$

with fixed parameters,  $\alpha = 0.5$ ,  $\delta = 0.1$ ,  $\epsilon = 0.25$ , and  $\omega = 2\pi/10$ . The canonical random variables  $\xi_1$ ,  $\xi_2$  and  $\xi_3$  are assumed to be independent, and uniformly distributed over the interval  $[-1, 1]$ .

Note that for  $\epsilon = 0$ , the flow is steady and one recovers the same formula as (27). For  $\epsilon > 0$  the flow is time-varying and the gyres undergo a periodic expansion and contraction in the  $x$ -direction, but such that the rectangular region enclosing the gyres remains fixed. The value of  $\epsilon$  determines the amplitude of the left-right motion of the line separating the gyres (Shadden et al. 2005),  $T = 2\pi/\omega$  is the period of the motion, whereas  $\alpha$  and  $\delta$  quantify the variability in the current velocity and in the gyre location.

The initial vehicle position and target are set to  $(t_0, x_0, y_0) = (0, -1, 0.25)$ , and  $(x_f, y_f) = (0.5, 0.5)$ , respectively. We consider a small vehicle speed,  $V = 0.75$ , leading to a stringent case for the optimization algorithm and statistical analysis. Consistent with our methodology above, a LHS strategy is used to generate an initial ensemble of flow realizations, and then rely on independent larger size ensembles to further assess the robustness of our estimates. To analyze the effect of the initial sample selection, we consider two independent 64-member ensembles, and perform the analysis for individual paths determined in each ensemble.

As in the steady example, we start by analyzing whether individual paths remain realizable when tested against current realizations belonging to the initial ensemble. For ensemble 1 we find 13 realizable paths, whereas 12 paths are found to be realizable in ensemble 2. The initial characterization of the arrival times are shown in Fig. 13(a) and 14(a), respectively. Plotted are estimates of the mean arrival time, the corresponding standard deviation,  $\sigma$ , the most likely travel time, and  $T^{95\%}$ . Next, these paths are re-evaluated against two independent LHS of the current field, comprising 144 and 256 members. For ensemble 1, we find that only 6 of the original 13 paths remain realizable (path 1, 2, 7, 8, 9, 11 in Fig. 13(b)), where for ensemble 2, we find that in 11 of 12 original paths remain realizable (path 2-12 in Fig. 14(b)).

To examine the impact of the selected parameters, Fig. 15 shows instantaneous snapshots of the velocity field, for two realizations of the germ,  $\boldsymbol{\xi}$ . The figures clearly illustrate the large variability in the current field with uncertain inputs, as well as their large time variation over the vehicle travel time. (Note that the snapshots span a time period that is comparable to the vehicle travel time.) The figures also illustrate that the vehicle travel distance and the uncertainty in gyre location both scale with the mean gyre radius. Due to these large variabilities,

the individual optimal trajectories, illustrated in Fig. 16(a) and 16(b) for the two ensembles considered, exhibit wider spread and more pronounced sensitivities to the random inputs.

We next focus on the paths minimizing the value at risk, as estimated based on  $T^{95\%}$ . For ensemble 1, this corresponds to path 1 in Fig. 13(b), while for ensemble 2, this corresponds to path 2 in Fig. 14(b). The pdf of the arrival times for these two paths are plotted in Fig. 13(c) and Fig. 14(c) respectively. Note that for both paths, the pdf's describe ranges that are comparable. Figure 17 contrasts the two paths resulting from ensembles 1 and 2. Though evidently not identical, the two paths are quite close to each other. The corresponding estimates of the values at risk are also comparable,  $T^{95\%} \simeq 1.85$  for the path selected based on ensemble 1, and  $T^{95\%} \simeq 1.8$  for the path selected based on ensemble 2. This indicates that for the present considered scenario, the size of the initial ensemble is sufficiently large for selecting a suitable path.

## 6 Conclusions

We developed an ensemble-based approach for path planning in uncertain flows. The approach is based on generating a finite-size ensemble of the current field, and applying well-established deterministic solvers to determine time-optimal paths corresponding to individual members of the current ensemble. Specifically, for each realization of the uncertain current field, we rely on a Hamiltonian formalism based on Pontryagin maximum principle to determine the corresponding optimal path. This leads to a bvp optimization problem, that is solved iteratively in order to predict the optimal path and to calculate the corresponding arrival time. Suitable initial guesses for the bvp solver are generated from a family of backward-in-time trajectories starting at the end position. The optimal solution predicted by the bvp solver is finally verified through forward integration using the corresponding steering law.

A functional representation of the uncertain current field is adopted, namely in terms of canonical, iid random variables. To mimic the situation of operational forecasts, a finite size ensemble of current fields is generated through LHS sampling of these random variables. The optimal paths corresponding to these individual realizations are then evaluated against members of the same ensemble. A path following law is used to determine whether an individual path remains realizable for different members of the current field ensemble, and in this case to characterize the corresponding travel time. This yields initial estimates of arrival time distribution for realizable paths, which are then evaluated using independent, larger ensembles. In particular, this approach readily provides estimates of the mean travel time, the corresponding standard deviation, the most likely travel time and the value at risk. The latter is in particular used as metric for path selection in the random field.

The presently-developed methodology is illustrated through applications to uncertain, canonical, 2D, steady and unsteady, double-gyre flows. The uncertainty is represented in terms of a low-dimensional random vector, affecting the direction and magnitude of the current field. Attention is first focused on the steady-state case, and two scenarios are considered corresponding to small and large vehicle speed. In the first scenario, simulations indicate that not all of the paths generated

by the initial ensemble remain realizable when tested against different members of the same ensemble. Consideration of larger, independent, current-field ensembles leads to additional elimination of initially realizable paths, including the path initially achieving by the best worst-case arrival time. This generally highlights the importance to suitably assess the variability in the current field. For the set of realizable paths, the analysis indicates that with suitably large ensembles, relevant statistics of the arrival time can be obtained. In particular, for the path characterized by the smallest value at risk, the arrival time distribution exhibits a large variability. In contrast, when the vehicle velocity is large, variability in the current field has essentially no impact on realizability of individual paths, and an appreciably smaller impact on the variability in arrival times.

The uncertainty analysis is finally applied to the case of a strong, unsteady, double-gyre flow. In particular, this setup is used to examine the impact of the selection of the design ensembles. Two independent, equal-size ensembles are selected for this purpose. Systematic application of the methodology indicates that the paths determined based on both design ensembles are very close, with comparable estimates of the value at risk. This provides confidence in the suitability of the present approach at least for the present setting.

In the present work, we restricted our attention to canonical, 2D, steady and unsteady flows, vehicles moving at a constant velocity with respect to the current, and relied on a simplified methodology to determine path-following steering laws. Work is currently underway to generalize the methodology, particularly to accommodate 3D time-dependent motion, realistic ocean forecasts, and to accommodate closed-loop control laws. Whereas the presently-developed, ensemble-based methodology extends in a straightforward fashion to these complex settings, one may need to combine it with more elaborate deterministic optimization algorithms and risk-based path selection schemes. For instance, the presence of coastal regions, islands, and moving obstacles would require inclusion of constraints in the formulation of the optimization problem, which may favor consideration of alternative strategies. An additional hurdle that must be addressed in a complex ocean settings concerns the possibility that none of individual trajectories remains realizable when tested against other members of the ensemble. This would motivate consideration of more sophisticated risk metrics, particularly to accommodate less risk-averse planning strategies. Establishment of such capabilities is the focus of ongoing research that will be reported elsewhere.

**Acknowledgements** This work was supported in part by the Uncertainty Quantification Center at King Abdullah University of Science and Technology.

## Appendices

### A Hamiltonian and adjoint equations for the steady, stochastic double gyre flow

For the velocity field in section 5.1, the Hamiltonian is expressed as:

$$\begin{aligned}
 H = & 1 + p_1 (-\sin(\pi x) \cos(\pi y) + V \cos \theta - \alpha \xi_1 \sin(\pi(x + \delta \xi_2)) \cos(\pi(y + \delta \xi_3))) \\
 & + p_2 (\cos(\pi x) \sin(\pi y) + V \sin \theta + \alpha \xi_1 \cos(\pi(x + \delta \xi_2)) \sin(\pi(y + \delta \xi_3))). \quad (32)
 \end{aligned}$$

and the adjoint equations for the extended system are:

$$\begin{aligned}\dot{p}_1 &= -\frac{\partial H}{\partial x} = p_1\pi \cos(\pi x) \cos(\pi y) + p_1\pi\alpha\xi_1 \cos(\pi(x + \delta\xi_2)) \cos(\pi(y + \delta\xi_3)) \\ &\quad + p_2\pi\alpha\xi_1 \sin(\pi(x + \delta\xi_2)) \sin(\pi(y + \delta\xi_3)) + p_2\pi \sin(\pi x) \sin(\pi y), \\ \dot{p}_2 &= -\frac{\partial H}{\partial y} = -p_1\pi \sin(\pi x) \sin(\pi y) - p_1\pi\alpha\xi_1 \sin(\pi(x + \delta\xi_2)) \sin(\pi(y + \delta\xi_3)) \\ &\quad - p_2\pi\alpha\xi_1 \cos(\pi(x + \delta\xi_2)) \cos(\pi(y + \delta\xi_3)) - p_2\pi \cos(\pi x) \cos(\pi y).\end{aligned}\quad (33)$$

## B Hamiltonian and adjoint equations for the unsteady, stochastic double gyre flow

For the velocity field in section 5.2, the Hamiltonian is:

$$\begin{aligned}H &= 1 + p_1(-\sin(\pi f(x, t)) \cos(\pi y) + V \cos \theta - \alpha\xi_1 \sin(\pi f(x + \delta\xi_2, t)) \cos(\pi(y + \delta\xi_3))) \\ &\quad + p_2(\alpha\xi_1 \cos(\pi f(x + \delta\xi_2, t)) \sin(\pi(y + \delta\xi_3)) (2a(t)(x + \delta\xi_2) + b(t)) + V \sin \theta) \\ &\quad + p_2 \cos(\pi f(x, t)) \sin(\pi y) (2a(t)x + b(t))\end{aligned}\quad (34)$$

and the costate equations for the extended system are given by:

$$\begin{aligned}\dot{p}_1 &= -\frac{\partial H}{\partial x} = p_1\pi \cos(\pi f(x, t)) \cos(\pi y) (2a(t)x + b(t)) \\ &\quad + p_1\pi\alpha\xi_1 \cos(\pi f(x + \delta\xi_2, t)) \cos(\pi(y + \delta\xi_3)) (2a(t)(x + \delta\xi_2) + b(t)) \\ &\quad + p_2\pi \sin(\pi f(x, t)) \sin(\pi y) (2a(t)x + b(t))^2 + 2p_2a(t) \cos(\pi f(x, t)) \sin(\pi y) \\ &\quad + p_2\pi\alpha\xi_1 \sin(\pi f(x + \delta\xi_2, t)) \sin(\pi(y + \delta\xi_3)) (2a(t)(x + \delta\xi_2) + b(t))^2 \\ &\quad + 2p_2\alpha\xi_1 a(t) \cos(\pi f(x + \delta\xi_2, t)) \sin(\pi(y + \delta\xi_3)), \\ \dot{p}_2 &= -\frac{\partial H}{\partial y} = -p_1\pi \sin(\pi f(x, t)) \sin(\pi y) - p_1\pi\alpha\xi_1 \sin(\pi f(x + \delta\xi_2, t)) \sin(\pi(y + \delta\xi_3)) \\ &\quad - p_2\pi \cos(\pi f(x, t)) \cos(\pi y) (2a(t)x + b(t)) \\ &\quad - p_2\pi\alpha\xi_1 \cos(\pi f(x + \delta\xi_2, t)) \cos(\pi(y + \delta\xi_3)) (2a(t)(x + \delta\xi_2) + b(t))\end{aligned}\quad (35)$$

At the final time,  $t = \bar{t}_f$ , the velocity components are:

$$u_f = -\sin(\pi f(x_f, \bar{t}_f)) \cos(\pi y_f) - \alpha\xi_1 \sin(\pi f(x_f + \delta\xi_2, \bar{t}_f)) \cos(\pi(y_f + \delta\xi_3))$$

and

$$\begin{aligned}v_f &= \cos(\pi f(x_f, \bar{t}_f)) \sin(\pi y_f) (2a(\bar{t}_f)x_f + b(\bar{t}_f)) \\ &\quad + \alpha\xi_1 \cos(\pi f(x_f + \delta\xi_2, \bar{t}_f)) \sin(\pi(y_f + \delta\xi_3)) (2a(\bar{t}_f)(x_f + \delta\xi_2) + b(\bar{t}_f)).\end{aligned}$$

Note that in the time-dependent case, the final time  $t_f$  is not known a priori. For the purpose of backward integration, the travel time at the end point is required to determine current. To overcome this difficulty, we introduce a guess  $\bar{t}_f \in [t_0, t_0 + T^{\max}]$  for the real travel time, where  $T^{\max}$  is the maximum time horizon. The guess for the final time is initialized using  $\bar{t}_f = t_0 + T^{\max}$ , and then sequentially reduced, as needed, until a convergent solution is reached.

## References

- Adhami-Mirhosseini A, Yazdanpanah MJ, Aguiar AP (2014) Automatic bottom-following for underwater robotic vehicles. *Automatica* 50(8):2155-2162
- Aguiar AP, Hespanha JP, Kokotović PV (2005) Path-Following for Nonminimum Phase Systems Removes Performance Limitations. *IEEE Trans Autom Control* 50(2):234-239

- Aguiar AP, Hespanha JP (2007) Trajectory-tracking and path-following of underactuated autonomous vehicles with parametric modeling uncertainty. *IEEE Trans Autom Control* 52(8):1362-1379
- Aguiar AP, Hespanha JP, Kokotović PV (2008) Performance limitations in reference tracking and path following for nonlinear systems. *Automatica* 44:598-610
- Aguiar AP, Pascoal AM (2007) Dynamic positioning and way-point tracking of underactuated AUVs in the presence of ocean currents. *Int J Control* 80(7):1092-1108
- Alexanderian A., Winokur J., Sraj I., Srinivasan A., Iskandarani M., Thacker W.C., Knio M.O. (2012) Global sensitivity analysis in an ocean general circulation model: a sparse spectral projection approach. *Comput Geosci* 16:757-778
- Bakolas E, Tsiotras P (2012) Feedback navigation in an uncertain flowfield and connections with pursuit strategies. *J Guid Control Dynam*, 35(4):1268-1279
- Betts JT (1998) Survey of numerical methods for trajectory optimization. *J Guid Control Dynam*, 21(2):193-207
- Bovio E, Cecchi D, Baralli F (2006) Autonomous underwater vehicles for scientific and naval operations. *Annu Rev Control* 30(2):117-130
- Bryson AE and Ho YC (1975) *Applied optimal control: optimization, estimation, and control*. CRC Press, New York
- Bakolas E, Tsiotras P (2010) The Zermelo-Voronoi diagram: A dynamic partition problem. *Automatica* 46:2059-2067
- Constantinescu EM, Zavala VM, Rocklin M, Lee S, Anitescu M (2011) A computational framework for uncertainty quantification and stochastic optimization in unit commitment with wind power generation. *IEEE Trans Power Syst* 26(1):431-441
- Eichhorn M (2015) Optimal routing strategies for autonomous underwater vehicles in time-varying environment. *Robot Auton Syst* 67:33-43
- Evensen G (2003) The Ensemble Kalman Filter: theoretical formulation and practical implementation. *Ocean Dynamics* 53(4):343-367
- Fainshil L, Margaliot M (2012) A maximum principle for the stability analysis of positive bilinear control systems with applications to positive linear switched systems. *SIAM J. Control Optim* 50(4):2193-2215
- Garau B, Alvarez A, Oliver G (2005) Path planning of autonomous underwater vehicles incur-rent fields with complex spatial variability: an A\* approach. In *Proceedings of the 2005 IEEE International Conference on Robotics and Automation*, pp 194-198
- Ghabcheloo R, Aguiar AP, Pascoal A, Silvestre C, Kaminer I, Hespanha J (2009) Coordinated path-following in the presence of communication losses and time delays. *SIAM J Control Optim* 48(1):234-265
- Gómez JV, Lumbier A, Garrido S, Moreno L (2013) Planning robot formations with fast marching square including uncertainty conditions. *Robot Auton Syst* 61:137-152
- Höllt Thomas, Hadwiger Markus, Knio O, Hoteit I (2015) Probability Maps for the Visualization of Assimilation Ensemble Flow Data. *Proceedings of Workshop on Visualisation in Environmental Sciences (EnvirVis)*, doi:10.2312/envirvis.20151090
- Hoteit I, Hoar T, Gopalakrishnan G, Collins N, Anderson J, Cornuelle B, Köhl A, Heimbach P (2013) A MITgcm/DART ensemble analysis and prediction system with application to the Gulf of Mexico. *Dynamics of Atmospheres and Oceans* 63:1-23
- Isern-González J, Hernández-Sosa D, Fernández-Perdomo E, Cabrera-Gómez J, Domínguez-Brito AC, Prieto-Marañón V (2012) Obstacle avoidance in underwater glider path planning. *J Phys Agents* 6(1):11-20
- Kaminer I, Pascoal A, Xargay E, Hovakimyan N, Cao C, Dobrokhodov V (2010) Path following for unmanned aerial vehicles using  $\mathcal{L}_1$  adaptive augmentation of commercial autopilots. *J Guid Control Dynam*, 33(2):550-564
- Kothari M, Postlethwaite I (2013) A probabilistically robust path planning algorithm for UAVs using rapidly-exploring random trees. *J Intell Robot Syst*, 71:231-253
- Lapierre L and Jouvencel B (2008) Robust nonlinear path-following control of an AUV. *IEEE J Ocean Eng*, 33(2):89-102
- Laschov D, Margaliot M (2013) Minimum-time control of boolean networks. *SIAM J. Control Optim*, 51(4):2869-2892
- Le Maître OP, Knio OM (2010) *Spectral methods for uncertainty quantification: with applications to computational fluid dynamics*. Springer-Verlaga, New York
- Lermusiaux PFJ, Chiu CS, Gawarkiewicz GG, Abbot P, Robinson AR, Miller RN, Haley PJ Jr., Leslie WG, Majumdar SJ, Pang A, Lekien F (2006) Quantifying uncertainties in ocean

- predictions. *Oceanography* 19(1):90-103
- Lermusiaux PFJ, Lolla T, Haley PJ Jr., Yigit K, Ueckermann MP, Sondergaard T, Leslie WG (2014) Science of Autonomy: timeoptimal path planning and adaptive sampling for swarms of ocean vehicles. Chapter 11, Springer Handbook of Ocean Engineering: Autonomous Ocean Vehicles, Subsystems and Control, Tom Curtin (Ed.) in press.
- Leutbecher M and Palmer TN (2008) Ensemble forecasting. *J Comput Phys* 227:3515-3539
- Liberzon D (2012) Calculus of variations and optimal control theory: a concise introduction. Princeton University Press, Princeton
- Lifshitz D, Weiss G (2015) Optimal control of a capacitor-type energy storage system. *IEEE Trans Autom Control* 60(1):216-220
- Lolla T, Haley PJ Jr., Lermusiaux PFJ (2014b) Time-optimal path planning in dynamic flows using level set equations: realistic applications. *Ocean Dyn* 64:1399-1417
- Lolla T, Lermusiaux PFJ, Ueckermann MP, Haley PJ Jr. (2014a) Time-optimal path planning in dynamic flows using level set equations: theory and schemes. *Ocean Dyn* 64:1373-1397
- Lolla T, Ueckermann MP, Yigit K, Haley PJ Jr., Lermusiaux PFJ (2012) Path planning in time dependent flow fields using level set methods. In Proceedings of IEEE International Conference on Robotics and Automation, pp. 166-173
- Longuski JM, Guzmán JJ, Prussing JE (2014) Optimal control with aerospace applications. Springer-Verlaga, New York
- McKay M, Conover W, Beckman R (1979) A comparison of three methods for selecting values of input variables in the analysis of output from a computer code. *Technometrics* 21: 239-245
- Marani G, Choi SK, Yuh J (2009) Underwater autonomous manipulation for intervention missions AUVs. *Ocean Eng* 36:15-23
- Marino A, Antonelli G, Aguiar AP, Pascoal A, Chiaverini S (2015) A decentralized strategy for multirobot sampling/patrolling: theory and experiments. *IEEE Trans Control Syst Technol* 23(1):313-322
- Murphy JM, Sexton DMH, Barnett DN, Jones GS, Webb MJ, Collins M, Stainforth DA (2004) Quantification of modelling uncertainties in a large ensemble of climate change simulations. *Nature* 430:768-772
- Ohsawa T (2015) Contact geometry of the Pontryagin maximum principle. *Automatica* 55:1-5
- Pereira A, Binney J, Hollinger GA, Sukhatme GS (2013) Risk-aware path planning for autonomous underwater vehicles using predictive ocean models. *J Field Robot* 30(5):741-762
- Pétrès C, Pailhas Y, Patrón P, Petillot Y, Evans J, Lane D (2007) Path planning for autonomous underwater vehicles. *IEEE Trans Robot* 23(2):331-341
- Rao AV (2009) Survey of numerical methods for optimal control. *Adv Astronaut Sci* 135(1):497-528
- Rao D and Williams SB (2009) Large-scale path planning for Underwater Gliders in ocean currents. In: Australasian Conference on Robotics and Automation (ACRA)
- Rhoads B, Mezić I, Poje A (2010) Minimum time feedback control of autonomous underwater vehicles. In Proceedings of 49th IEEE Conference on Decision and Control, pp 5828-5834
- Rhoads B, Mezić I, Poje AC (2013) Minimum time heading control of underpowered vehicles in time-varying ocean currents. *Ocean Eng* 66:12-31
- Sapsis TP, Lermusiaux PFJ (2009) Dynamically orthogonal field equations for continuous stochastic dynamical systems. *Physica D* 238:2347-2360
- Sapsis TP, Lermusiaux PFJ (2012) Dynamical criteria for the evolution of the stochastic dimensionality in flows with uncertainty. *Physica D* 241:60-76
- Sethian JA (1999a) Fast marching methods. *SIAM Rev* 41(2):199-235
- Sethian JA (1999b) Level set methods and fast marching methods: evolving interfaces in computational geometry, fluid mechanics, computer vision, and materials Science. Cambridge University Press, Cambridge
- Sethian JA, Vladimirsky A (2001) Ordered upwind methods for static Hamilton-Jacobi equations. *Proc Natl Acad Sci USA* 98(20):11069-11074.
- Sethian JA, Vladimirsky A (2003) Ordered upwind methods for static Hamilton-Jacobi equations: theory and algorithm. *SIAM J Numer Anal* 41(1):325-363
- Shadden SC, Lekien F, Marsden JE (2005) Definition and properties of Lagrangian coherent structures from finite-time Lyapunov exponents in two-dimensional aperiodic flows. *Phys D* 212:271-304
- Smith RN, Huynh VT (2014) Controlling buoyancy-driven profiling floats for applications in ocean observation. *IEEE J Oceanic Eng* 39(3):571-586

- Soulignac M (2011) Feasible and optimal path planning in strong current fields. *IEEE Trans Robot* 27(1):89-98.
- Sraj I., Iskandarani M., Srinivasan A., Thacker W.C., Winokur J., Alexanderian A., Lee C.-Y., Chen S.S., Knio O.M. (2013) Bayesian inference of drag parameters using AXBT data from Typhoon Fanapi. *Mon Wea Rev* 141: 2347-2367.
- Sraj I., Iskandarani M., Thacker C., Srinivasan A., Knio O.M. (2014) Drag parameter estimation using gradients and Hessian from a polynomial chaos model surrogate. *Mon Wea Rev* 142: 933-941.
- Sraj I., Mandli K.T., Knio O.M., Dawson C.N., Hoteit I. (2014) Uncertainty quantification and inference of Mannings friction coefficients using DART buoy data during the Tōhoku tsunami. *Ocean Model* 83: 82-97.
- Sujit PB, Saripalli S, Sousa JB (2011) Unmanned aerial vehicle path following: a survey and analysis of algorithms for fixed-wing Unmanned Aerial Vehicles. *IEEE Control Syst Mag* 34(1):42-59.
- Techy L and Woolsey CA (2009) Minimum-time path planning for unmanned aerial vehicles in steady uniform winds. *J Guid Control Dynam*, 32(6):1736-1746
- Wang D, Lermusiaux PFJ, Haley PJ, Eickstedt D, Leslie WG, Schmidt H (2009) Acoustically focused adaptive sampling and on-board routing for marine rapid environmental assessment. *J Mar Syst* 78:S393-S407
- Wolf MT, Blackmore L, Kuwata Y, Newman C (2010) Probabilistic motion planning of balloons in strong, uncertain wind fields. In *Proceedings of 2010 IEEE International Conference on Robotics and Automation*, pp 1123-1129
- Wu PY, Campbell D, Merz T (2011) Multi-objective four-dimensional vehicle motion planning in large dynamic environments. *IEEE Trans Syst, Man, Cybern B, Cybern*, 41(3):621-634
- Xargay E, Kaminer I, Pascoal A, Hovakimyan N, Dobrokhodov V, Cichella V, Aguiar AP, Ghabcheloo R (2013) Time-critical cooperative path following of multiple unmanned aerial vehicles over time-varying networks. *J Guid Control Dynam*, 36(2):499-516

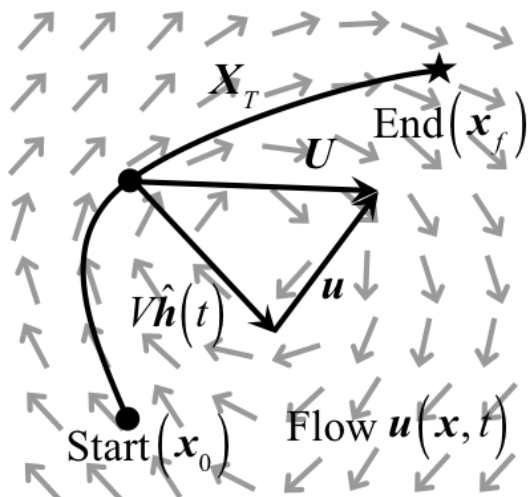


Fig. 1: Motion of P in a flow field  $u \equiv u(x, t)$ . Its trajectory  $X_T$  connects the start position,  $x_0$ , and the end position,  $x_f$ , and satisfies the kinematic relation (1) as well as the limiting conditions (2). The total velocity,  $U \equiv U(X_T, t)$ , is the vector sum of the flow velocity,  $u$ , and the steering velocity,  $V\hat{h}(t)$ .

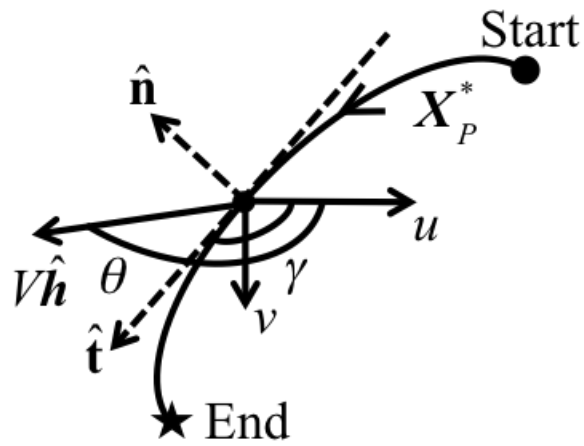


Fig. 2: Schematic showing the components of the local current velocity,  $(u, v)$ , the vehicle velocity vector,  $V\hat{h}$ , the vehicle heading,  $\hat{h}$ , the start position ( $\bullet$ ), the end position ( $\star$ ), and the unit tangent and normal to the trajectory,  $\hat{t}$  and  $\hat{n}$ , respectively. Also illustrated are the definitions of the angles  $\theta$  and  $\gamma$ .

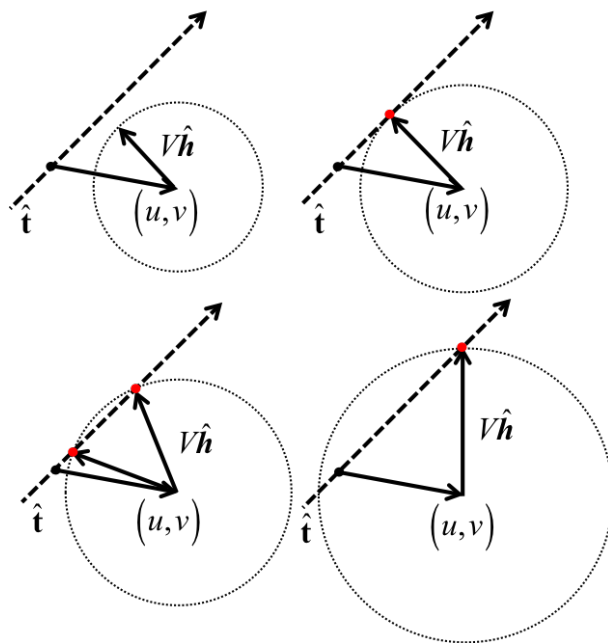


Fig. 3: Schematic showing the possible solutions for  $\theta$  according to different magnitudes of  $V$ .

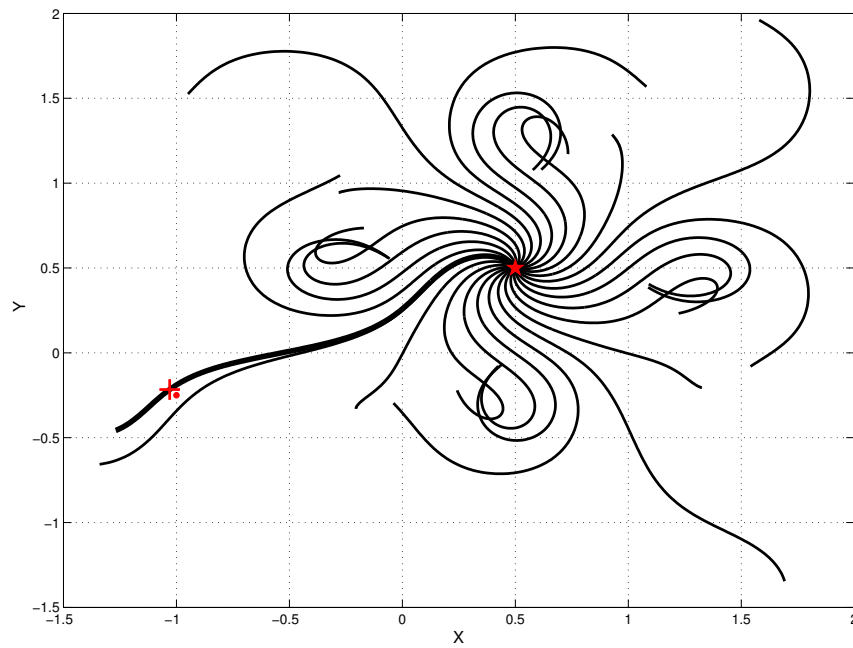


Fig. 4: Selected backward-in-time trajectories starting at the end position ( $\star$ ). A total of 360 trajectories is computed, but only 24 are shown. The backward integration is carried out for a time period of 2. The bold line is used to identify the trajectory that comes closest to the start position ( $\bullet$ ). The (+) sign is used to denote the point closest to the start in the whole ensemble.

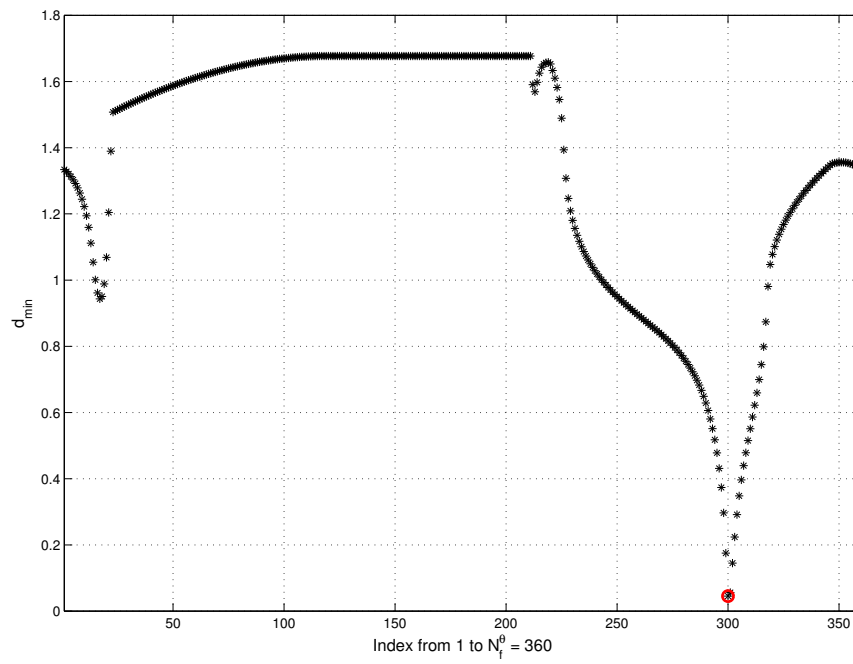


Fig. 5: The closest distance between each trajectory in the ensemble and the start position. The red dot ( $\circ$ ) is used to denote the overall minimum for the ensemble.

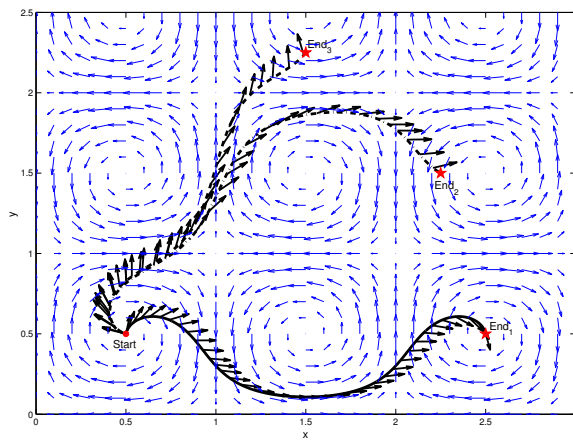


Fig. 6: Three optimal trajectories and the corresponding optimal control inputs for the time-invariant, spatially double-gyre flow. Note that the control vectors are sometimes tangential to the flow and sometimes normal.

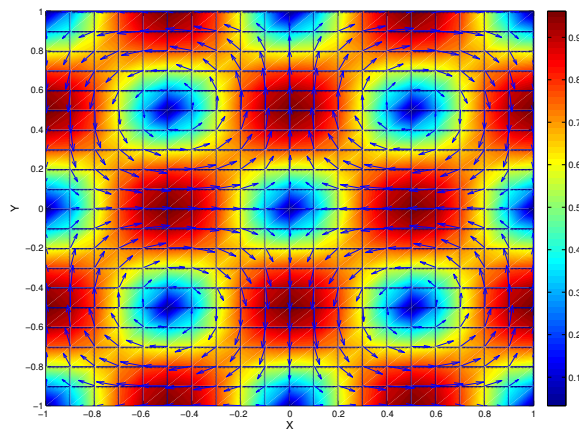
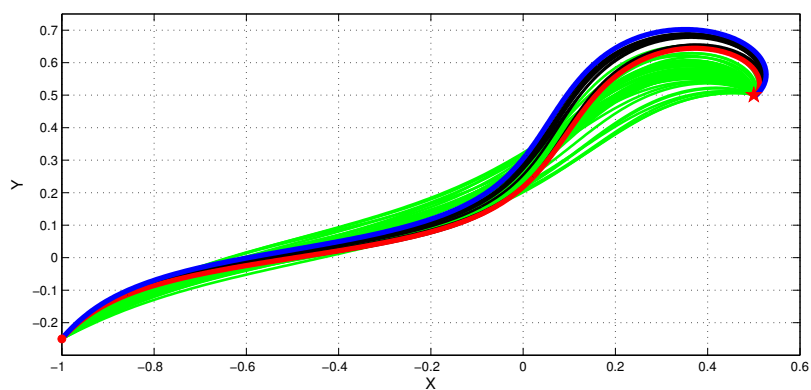
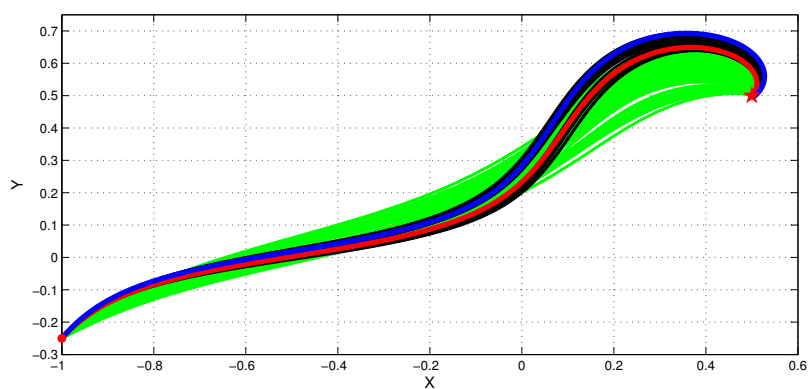


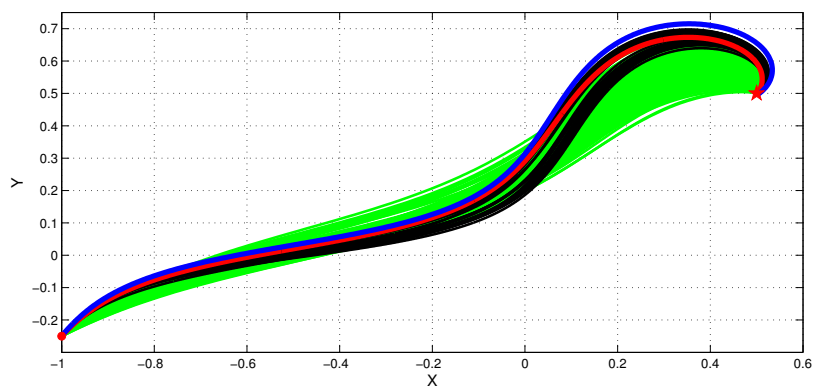
Fig. 7: The mean velocity vector estimated based on 64 pseudo-random samples of uncertain flow field. The local vectors are represented using arrows, whereas the colour contours reflect the mean velocity magnitude.



(a) The 64-member ensemble with 12 realizable paths.



(b) The 144-member ensemble with 26 realizable paths.



(c) The 256-member ensemble with 31 realizable paths.

Fig. 8: Deterministic trajectories in strong, uncertain flow field. The starting position is denoted using ( $\bullet$ ) and the end position is indicated using ( $\star$ ). The unrealizable trajectories are colored in green. The path having the best worst travel time is identified using a red, bold line. The path resulting in the longest worst travel time is plotted using blue, bold line. The remaining realizable paths are plotted using black lines.

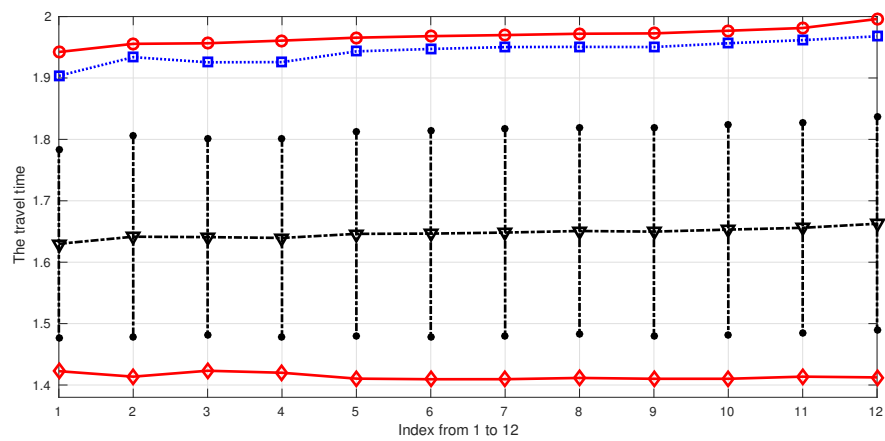
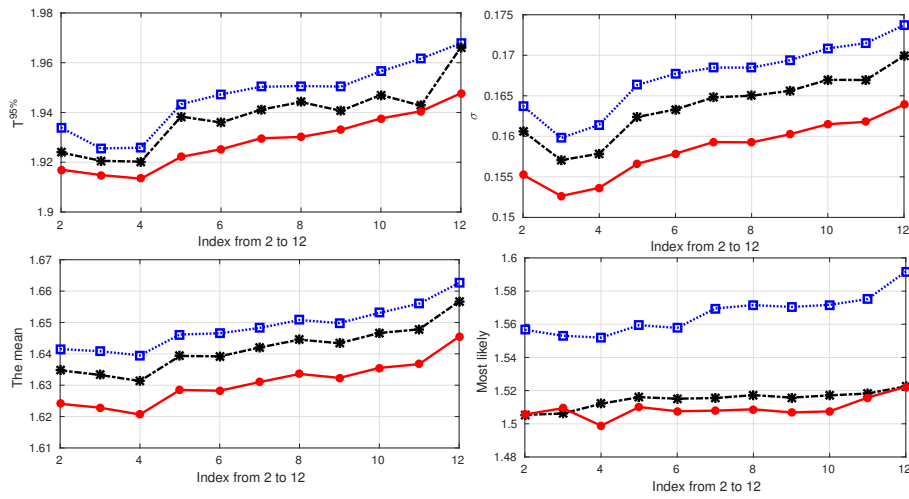
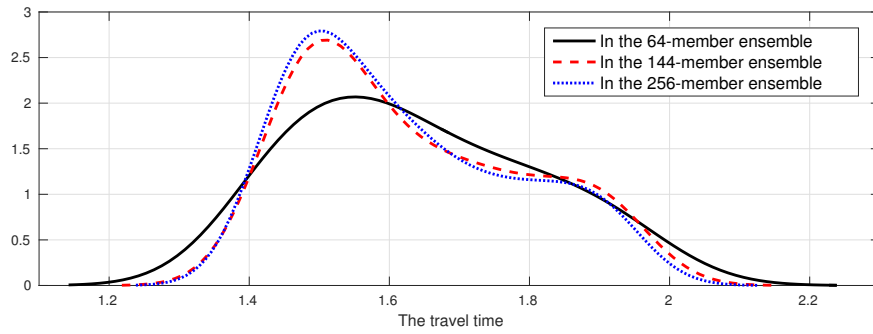


Fig. 9: Travel times of the realizable paths in strong, uncertain flow field for small  $V$ . Plotted are  $T^{worst}$  ( $\circ$ ),  $T^{95\%}$  ( $\square$ ), the mean  $\bar{T}$  ( $\nabla$ ), the  $\bar{T} \pm \sigma$  estimates ( $\bullet$ ) and  $T^{best}$  ( $\diamond$ ). The results are indexed in increasing order of  $T^{worst}$ . Results are shown based on the 64-member ensemble.



(a) Characterization of the travel times for the 11 realizable paths in the 64-member ensemble. Distributions are shown using the 64-member ensembles ( $\square$ ), the 144-member ensemble (\*), and the 256-member ensemble ( $\bullet$ ). The most likely travel time corresponds to the  $x$ -coordinate of the peak in pdf of the travel time distribution.



(b) The pdf of the travel time of the fourth realizable path in different-size ensembles.

Fig. 10: Travel time characterization of realizable paths, and pdf of the arrival time for the path with optimal  $T^{95\%}$ .

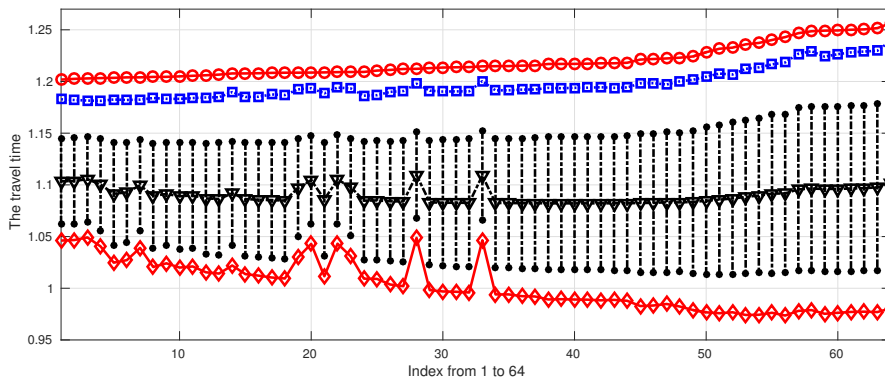
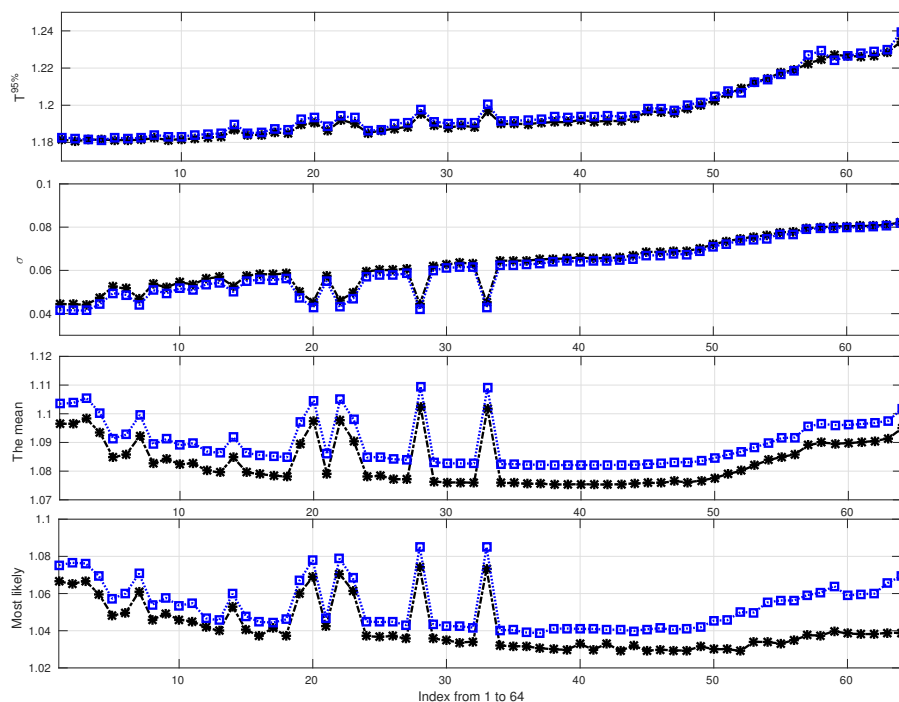
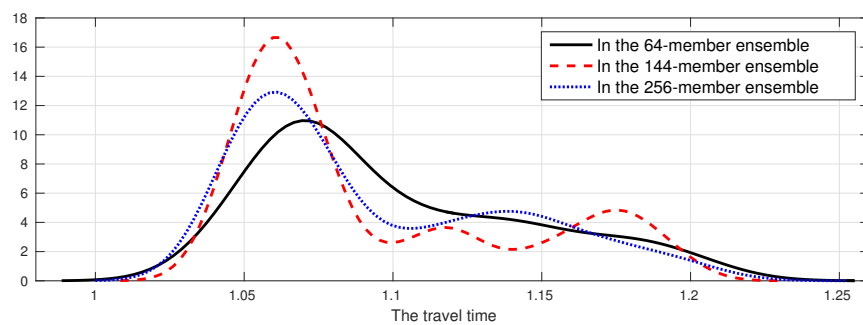


Fig. 11: Travel times of the realizable paths in strong, uncertain flow field for large  $V$ . Plotted are  $T^{worst}$  ( $\circ$ ),  $T^{95\%}$  ( $\square$ ), the mean  $\bar{T}$  ( $\nabla$ ), the  $\bar{T} \pm \sigma$  estimates ( $\bullet$ ) and  $T^{best}$  ( $\diamond$ ). The results are indexed in increasing order of  $T^{worst}$ . Results are shown based on the 64-member ensemble.

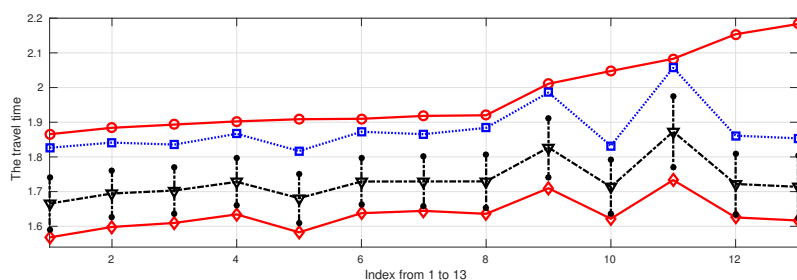


(a) Characterization of the travel times for the 64 realizable paths in the 64-member ensemble. Distributions are shown using the 64-member ensembles ( $\square$ ), and the 144-member ensemble (\*). The most likely travel time corresponds to the  $x$ -coordinate of the peak in pdf of the travel time distribution.

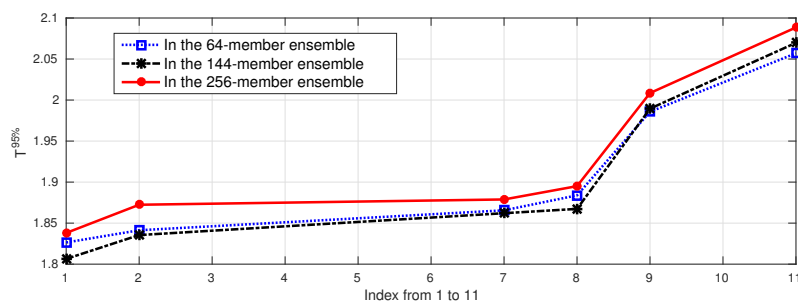


(b) The pdf of the travel time of the fourth realizable path in different-size ensembles.

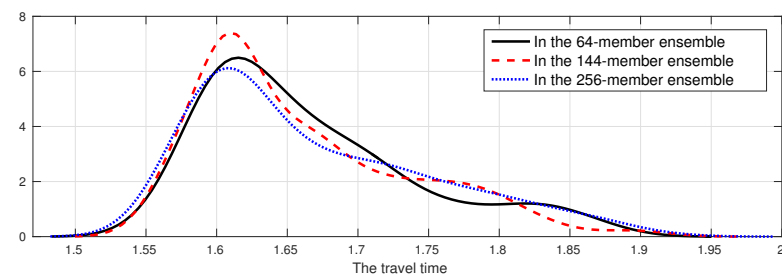
Fig. 12: Travel time characterization of realizable paths, and pdf of the arrival time for the path with optimal  $T^{95\%}$ .



(a)  $T^{worst}$  ( $\circ$ ),  $T^{95\%}$  ( $\square$ ),  $\bar{T}$  ( $\nabla$ ), and  $\bar{T} \pm \sigma$  estimates ( $\bullet$ ) for the unsteady double gyre flow. The predictions are arranged in increasing order of  $T^{worst}$ .

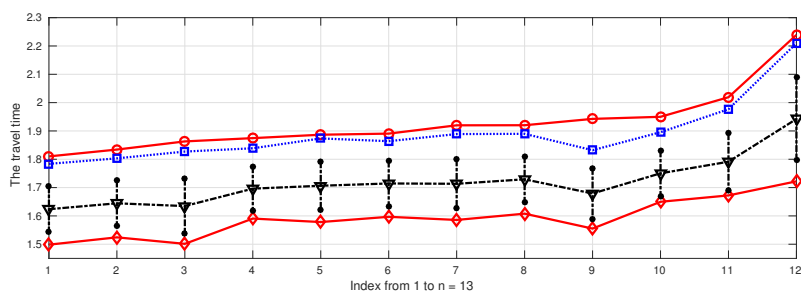


(b) Estimates of  $T^{95\%}$  for the 6 realizable paths. Plotted are estimates obtained using independent ensembles as shown in the labels.

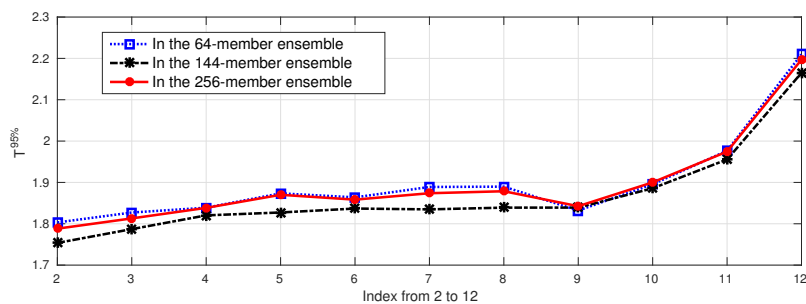


(c) Pdf of the travel time of the first realizable path in different-size ensembles.

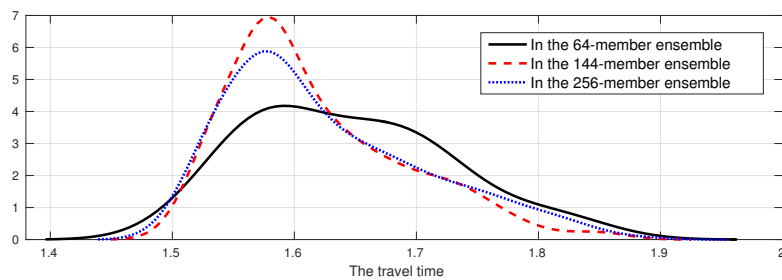
Fig. 13: Travel time characterization of realizable paths, and pdf of the arrival time for the path with optimal  $T^{95\%}$ . Results are based on realizable paths in ensemble 1.



(a)  $T^{worst}$  ( $\circ$ ),  $T^{95\%}$  ( $\square$ ),  $\bar{T}$  ( $\nabla$ ), and  $\bar{T} \pm \sigma$  estimates ( $\bullet$ ) for the unsteady double gyre flow. The predictions are arranged in increasing order of  $T^{worst}$ .



(b) Estimates of  $T^{95\%}$  for the 11 realizable paths. Plotted are estimates obtained using independent ensembles as shown in the labels.



(c) Pdf of the travel time of the second realizable path in different-size ensembles.

Fig. 14: Travel time characterization of realizable paths, and pdf of the arrival time for the path with optimal  $T^{95\%}$ . Results are based on realizable paths in ensemble 2.

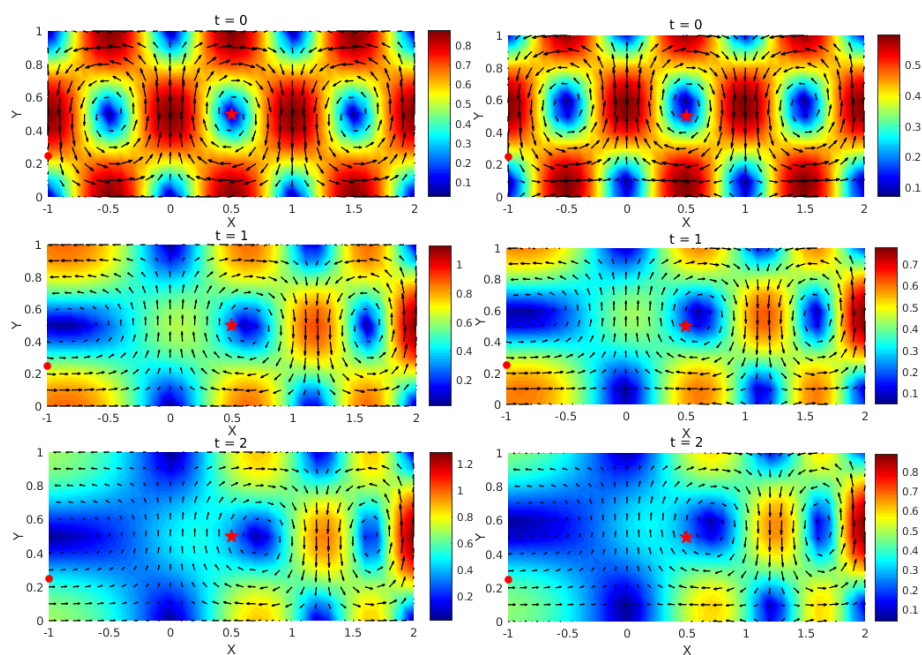
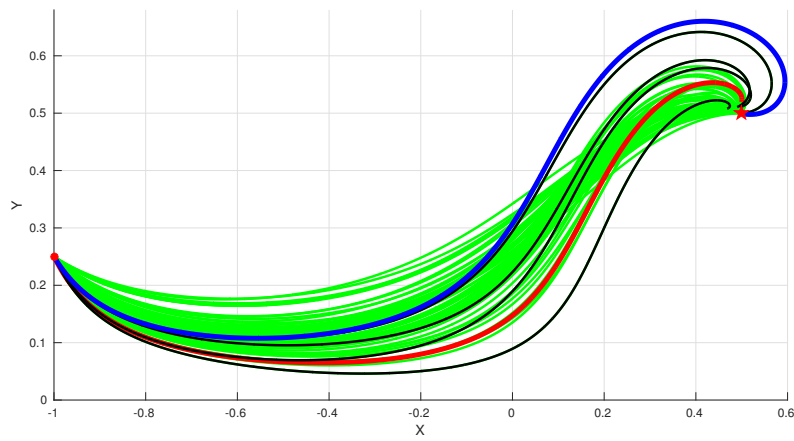
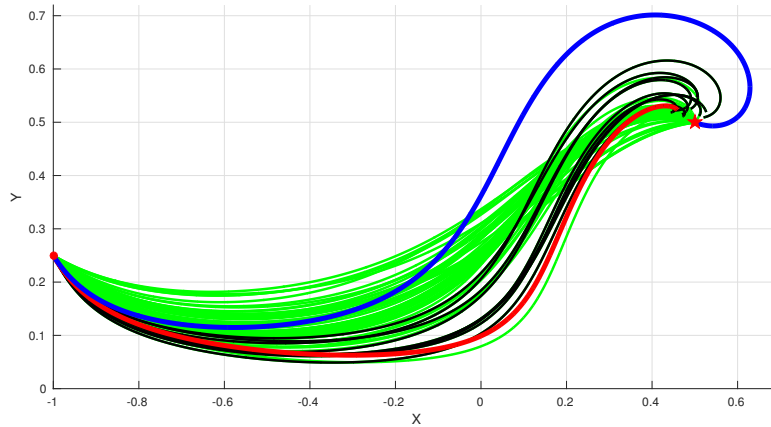


Fig. 15: Instantaneous snapshots of the double-gyre current field. The snapshots are generated at times  $t = 0, 1,$  and  $2$ , arranged from top to bottom. Two realizations of the germ are illustrated; left:  $\xi_1 = -0.2563, \xi_2 = 0.5194,$  and  $\xi_3 = -0.3457$ , right:  $\xi_1 = -0.18562, \xi_2 = -0.1370,$  and  $\xi_3 = 0.9271$ . The starting position is indicated using  $(\bullet)$  and the end position is indicated using  $(\star)$ . The local velocity field is represented using arrows, whereas the color contours reflect the velocity magnitude. Note that the scales differ for the two realizations.



(a) The 6 realizable paths in ensemble 1.



(b) The 11 realizable paths in ensemble 2.

Fig. 16: Deterministic trajectories in strong, unsteady, and uncertain flow field. The starting position is denoted using  $(\bullet)$  and the end position is indicated using  $(\star)$ . The unrealizable trajectories are colored in green. The path having the best worst travel time is identified using a red, bold line. The path resulting in the longest worst travel time is plotted using a blue, bold line. The remaining realizable paths are plotted using black lines.

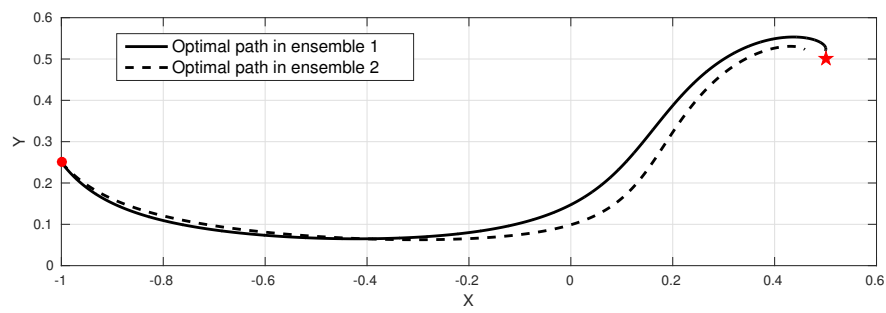


Fig. 17: The two optimal paths in uncertain time-dependent double-gyre flow. The starting position is denoted using ( $\bullet$ ) and the end position is indicated using ( $\star$ ). The curves correspond to predictions based on ensembles 1 and 2, as indicated.